Title
Vehicle Lateral Control Under Fault in Front and/or Rear Sensors: Final Report

Authors
Lu, Guang
Huang, Jihua
Tomizuka, Masayoshi

Publication Date
2004-09-01

CALIFORNIA PATH PROGRAM
INSTITUTE OF TRANSPORTATION STUDIES
UNIVERSITY OF CALIFORNIA, BERKELEY

Vehicle Lateral Control Under Fault in Front and/or Rear Sensors: Final Report

Guang Lu, Jihua Huang, Masayoshi Tomizuka
University of California, Berkeley

California PATH Research Report
UCB-ITS-PRR-2004-36

This work was performed as part of the California PATH Program of the University of California, in cooperation with the State of California Business, Transportation, and Housing Agency, Department of Transportation; and the United States Department of Transportation, Federal Highway Administration.

Final Report for Task Order 4204

September 2004

ISSN 1055-1425

CALIFORNIA PARTNERS FOR ADVANCED TRANSIT AND HIGHWAYS

PROJECT TITLE:

Vehicle Lateral Control under Fault in Front and/or Rear Sensors

By

Guang Lu
Jihua Huang
Masayoshi Tomizuka

Department of Mechanical Engineering
University of California at Berkeley
Berkeley, CA 94720

Final report for TO 4204

June 2004

Executive Summary

This report presents the research results of Task Order 4204(TO4204), *"Vehicle Lateral Control under Fault in Front and/or Rear Sensors"*. This project is a continuing effort of the Partners for Advanced Transit and Highways (PATH) on the research of passenger vehicles for Automated Highway Systems (AHS).

An AHS is an automatic control system designed for enhanced highway safety and throughput, with each vehicle controlled by an on-board computer in both longitudinal and lateral directions. The goal of vehicle lateral control is to keep the vehicle in the lane laterally by controlling the steering angle at the tires. PATH has adopted a magnetic road reference system, in which each automated lane has equally-spaced magnets buried underneath the centerline. Magnetometers on-board a vehicle sense the magnetic field generated by each magnet. The lateral controller calculates the lateral deviation from the outputs of the magnetometers and uses this information to set the steering command.

Current PATH vehicle lateral controllers rely on the use of two sets of magnetometers on-board each vehicle, one under the front bumper, and the other under the rear bumper. Failure of magnetometers will lead to degraded mode operation and can potentially be a safety hazard. As part of an overall effort to build a reliable fault management system, TO4204 addresses the problem of developing degraded mode vehicle lateral control strategies. TO4204 is the first research project to systematically study vehicle lateral control strategies under faulty operation of the magnetometers. This project is primarily concerned with the following problems.

- lateral control of the vehicle using only one set of magnetometers
- autonomous lateral control based on a laser scanning radar sensor (LIDAR) (without the use of magnetometers)

Analysis on the vehicle lateral dynamics indicates that the system zeros become weakly damped when rear magnetometers fail and a Right-Half-Plane (RHP) zero

appears when front mangetometers fail. In addition, the vehicle lateral dynamics during magnetometer failures becomes more sensitive to the changes of the longitudinal velocity and has to be treated as a Linear Time Varying (LTV) system.

Two methods are employed in the degraded mode controller design using only one set of magnetometers. The first method combines H_∞ optimal control with gain scheduling. The main idea is to achieve stronger robustness to variation of vehicle velocity by combining several robust H_∞ controllers. The second method combines feedback linearization with a mismatched observer. Feedback linearization provides a simple and effecive way of gain scheduling and the mismatch observer prevents the weakly damped zeros or the RHP zero of the vehicle lateral dynamics from being contained in the internal dynamics. To ensure the success of the fault management system, the transition behavior between the normal mode control and the degraded mode control is also investigated.

When all the magnetometers fail, autonomous vehicle following allows a vehicle to automatically follow its preceding vehicle based on the measurements of the relative distance between the two vehicles. If the leading vehicle tracks the road centerline reasonably well, this approach can achieve good lane-keeping performance of the controlled vehicle without using any road reference frame. The relative distance is measured by an on-board laser scanning radar (LIDAR) sensor. Propagation of errors from one vehicle to another is highly concerned as the platoon may become string unstable when it contains many vehicles. Analysis of string stability is performed, and inter-vehicle communication is suggested as a means to solve the string stability problem. Experimental results are used to show the effectiveness of the proposed solution.

Autonomous vehicle following may work as a back-up system for the magnetometer-based systems when the magnetometers are under partial failure. An integrated vehicle steering control scheme is proposed to combine the use of LIDAR and rear magnetometers. The solution is verified by both simulations and real-time testing.

Abstract

This report documents the findings of research performed under TO4204, *"Vehicle Lateral Control under Fault in Front and/or Rear Sensors"*. The research goal of TO4204 is to develop vehicle lateral control strategies under faulty operation of the magnetometers. The main objectives of the project are: (1) to design controllers that use the output from only one set of magnetometers, and (2) to develop an autonomous lateral control scheme that uses no magnetometers.

Two methods are employed in the degraded mode controller design using only one set of magnetometers. In the first method, H_∞ control with gain scheduling combines the robust performance range of several H_∞ controllers to achieve stronger robustness to the variation of vehicle velocity. The second method combines feedback linearization, which provides a simple and effecive way of gain scheduling, with mismatched observer, which prevents undesired zeros of the vehicle lateral dynamics from being contained in the internal dynamics. To ensure the success of the fault management system, transition behavior between the normal mode control and the degraded mode control is also investigated.

When all the magnetometers fail, autonomous vehicle following allows a vehicle to automatically follow its preceding vehicle based on information of the relative distance between the two vehicles. The relative distance is measured by an on-board laser scanning radar (LIDAR) sensor. One issue in autonomous vehicle following is a propagation of errors from one vehicle to another. When errors increase in the upstream direction of a vehicle platoon, the platoon is string unstable. Analysis of string stability is performed, and inter-vehicle communication is suggested as a means to solve the string stability problem. Since vehicle lateral control with rear magnetometers is more challenging, an integrated vehicle steering control scheme, which combines the use of LIDAR and rear magnetometers, is introduced. The solution is verified by both simulations and real-time testing.

Keywords: vehicle lateral control, H_∞ control, autonomous vehicle following.

Contents

1 Introduction

1.1 Motivation and Scope

This project focuses on vehicle lateral control subject to magnetometer failures. The current PATH lateral control algorithms rely on the outputs of two sets of magnetometers, one installed under the front bumper of the vehicle and the other under the rear bumper of the vehicle. Failures in these magnetometers lead to degraded mode operation, and can potentially be a safety hazard. TO4204 is the first research project to systematically study vehicle lateral control strategies under faulty operation of magnetometers. This project is a part of the fault management of vehicle lateral control in Automated Highway Systems. The main research topics concerned in this project are as follows.

- Developing lateral controllers that use only one set of magnetometers (when the other set of magnetometers fails).
- Developing autonomous vehicle following control schemes based on laser scanning radar sensor(LIDAR) that uses no magnetometers (when both sets of magnetometers fail).

1.2 Vehicle Lateral Dynamics and Sensor Location Analysis

For simplicity, this report considers only front-wheel-steered vehicles. For a single vehicle, the bicycle model is used for analysis and design of control laws. The model is depicted in Fig.1, where CG denotes the center of gravity of the vehicle and other variables and parameters are defined later. The lateral force generated through the road-tire interaction applies to the vehicle, and causes lateral motion. The model is based on the following assumptions[7].

- Roll, pitch or bounce motions are negligible.

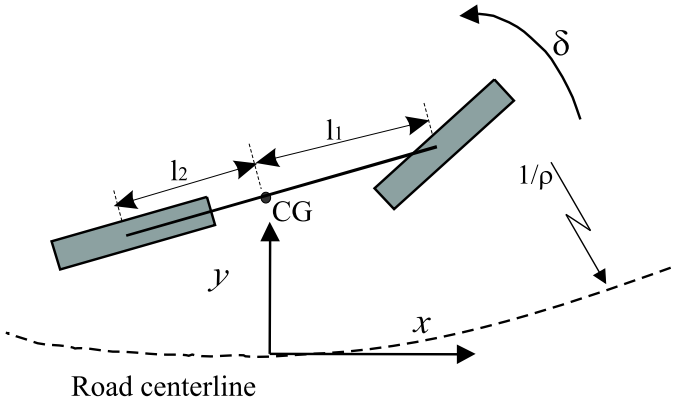

Figure 1: Bycicle model

- The relative yaw between vehicle and the road is small.
- The steering angle is small.
- The tire lateral force varies linearly with the slip angle.

Based on the above assumptions, the bicycle model in the road reference frame is:

$$m\ddot{y} = -m\dot{\epsilon}\dot{x} - \frac{C_{\alpha_r}(\dot{y} - \dot{\epsilon}l_2)}{\dot{x}} - \frac{C_{\alpha_f}(\dot{y} + \dot{\epsilon}l_1)}{\dot{x}} + C_{\alpha_f} \tag{1}$$

$$I_z\ddot{\epsilon} = l_2\frac{C_{\alpha_r}(\dot{y} - \dot{\epsilon}l_2)}{\dot{x}} - l_1\frac{C_{\alpha_f}(\dot{y} + \dot{\epsilon}l_1)}{\dot{x}} + l_1C_{\alpha_f} \tag{2}$$

where $\dot{x}$ and $\dot{y}$ are the components of the vehicle velocity along longitudinal and lateral principle axis of the vehicle body, $\dot{\epsilon}$ is the yaw rate, m and I_z are the mass and the yaw moment of inertia, respectively, l_1 and l_2 are respectively distances of the front and rear axle from CG, C_{α_f} and C_{α_r} represent the front and rear tire cornering stiffness, respectively, and δ is the steering angle. Equations 1 and 2 can also be written as,

$$\ddot{y_s} = f_1 + b_1\delta \tag{3}$$

$$\begin{aligned}\ddot{\epsilon_r} = \frac{l_1C_{\alpha_f} - l_2C_{\alpha_r}}{I_z\dot{x}}\dot{y_s} + \frac{l_1C_{\alpha_f} - l_2C_{\alpha_r}}{I_z}\epsilon_r + \frac{C_{\alpha_f}l_1}{I_z}\delta - \\ -\frac{C_{\alpha_f}({l_1}^2 - l_1d_s) + C_{\alpha_r}({l_2}^2 + l_2d_s)}{I_z\dot{x}}\dot{\epsilon_r} - \frac{C_{\alpha_f}{l_1}^2 + C_{\alpha_r}{l_2}^2}{I_z\dot{x}}\dot{\epsilon_d}\end{aligned} \tag{4}$$

where d_s is the distance between the measurement point and the vehicle CG, y_s represents the vehicle lateral error at the measurement point (either real or virtual), ϵ_r is the relative yaw angle, and f_1 and b_1 are given as follows.

$$f_1 = -\frac{\phi_1 + \phi_2}{\dot{x}}\dot{y}_s + (\phi_1 + \phi_2)\epsilon_r + \frac{\phi_1(d_s - l_1) + \phi_2(d_s + l_2)}{\dot{x}}\dot{\epsilon_r} + \frac{\phi_2 l_2 - \phi_1 l_1 - \dot{x}^2}{\dot{x}}\dot{\epsilon_d} \quad (5)$$

$$b_1 = \phi_1 \quad (6)$$

$$\phi_1 = C_{\alpha_f}(\frac{1}{m} + \frac{l_1 d_s}{I_z}) \quad (7)$$

$$\phi_2 = C_{\alpha_r}(\frac{1}{m} - \frac{l_2 d_s}{I_z}) \quad (8)$$

The state-space-form representation of these equations is

$$\dot{\xi} = A\xi + B\delta + W\rho \quad (9)$$

where

$$\xi = \begin{pmatrix} y_s & \dot{y}_s & \epsilon & \dot{\epsilon} \end{pmatrix}^T \quad (10)$$

$$A = \begin{pmatrix} 0 & 1 & 0 & 0 \\ 0 & -\frac{a_{11}}{\dot{x}} & a_{11} & \frac{a_{12}}{\dot{x}} \\ 0 & 0 & 0 & 1 \\ 0 & -\frac{a_{41}}{\dot{x}} & a_{41} & \frac{a_{42}}{\dot{x}} \end{pmatrix} \quad (11)$$

$$B = \begin{pmatrix} 0 \\ b_{21} \\ 0 \\ b_{41} \end{pmatrix} \quad (12)$$

$$W = \begin{pmatrix} 0 \\ w_{21} \\ 0 \\ w_{41} \end{pmatrix} \quad (13)$$

$$a_{11} = (\phi_1 + \phi_2), a_{12} = \phi_1(d_s - l_1) + \phi_2(d_s + l_2) \quad (14)$$

$$a_{41} = \frac{l_1 C_{\alpha_f} - l_2 C_{\alpha_r}}{I_z} \tag{15}$$

$$a_{42} = \frac{l_1 C_{\alpha_f}(d_s - l_1) + l_2 C_{\alpha_r}(d_s + l_2)}{I_z} \tag{16}$$

$$b_{21} = \phi_1, b_{41} = \frac{l_1 C\alpha_f}{I_z} \tag{17}$$

$$w_{21} = -\frac{{l_1}^2 C_{\alpha_f} + {l_2}^2 C_{\alpha_r}}{I_z} \tag{18}$$

$$w_{41} = \phi_2 l_2 - \phi_1 l_1 - \dot{x}^2 \tag{19}$$

and $\rho = \frac{\dot{\epsilon_d}}{\dot{x}}$ is the road curvature, which is treated as a disturbance in most lateral controller designs. The physical meaning and values of the symbols are listed in Table 1.

In the above description, the steering angle δ in the state-space equation is the control input. The control algorithm calculates the steering angle to generate the desired lateral force and hence the desired lateral motion so that the lateral deviation of the vehicle is regulated. The road curvature ρ is considered small for highway applications, and it is treated as disturbance in system analysis and controller design.

Note that the lateral deviation can be measured at any point of the vehicle, not necessarily at the vehicle's CG. Assuming that the sensor is located at distance d_s ahead of the vehicle's CG, the sensor output is

$$y_s = (\ 1 \quad 0 \quad d_s \quad 0\ )\xi \tag{20}$$

The position of the sensor determines the location of the system zeros of the transfer function from the steering input to the sensor output. At a fixed vehicle speed, the amount of phase lead increases as d_s increases (see Fig.2), which makes the system easy to stabilize. Because of this property, the steering control algorithms described in [6][7][11] employ a geometric look-ahead scheme, where the lateral error at some distance ahead of the vehicle CG, i.e. at a large d_s, is geometrically constructed from two sets of magnetometers (mounted under the front and rear bumpers) and used as the feedback signal. As shown in Fig.3, the virtual lateral error y_{vs} can be

Table 1: Vehicle Parameters

Symbols	Physical Meaning	Value
m	mass	$1485kg$
L	relative longitudinal distance between vehicles	$8m$
h_1	distance of front bumper to CG	$2.7m$
h_2	distance of rear bumper to CG	$2.1m$
d_s	distance of sensor location to CG	
	distance between vehicles	
I_z	yaw moment of inertia	$2872kg/m^2$
C_{α_f}	front wheel cornering stiffness	$42000N/rad$
C_{α_r}	rear wheel cornering stiffness	$42000N/rad$
l_1	distance between front wheel and the CG	$1.1m$
l_2	distance between rear wheel and the CG	$1.58m$

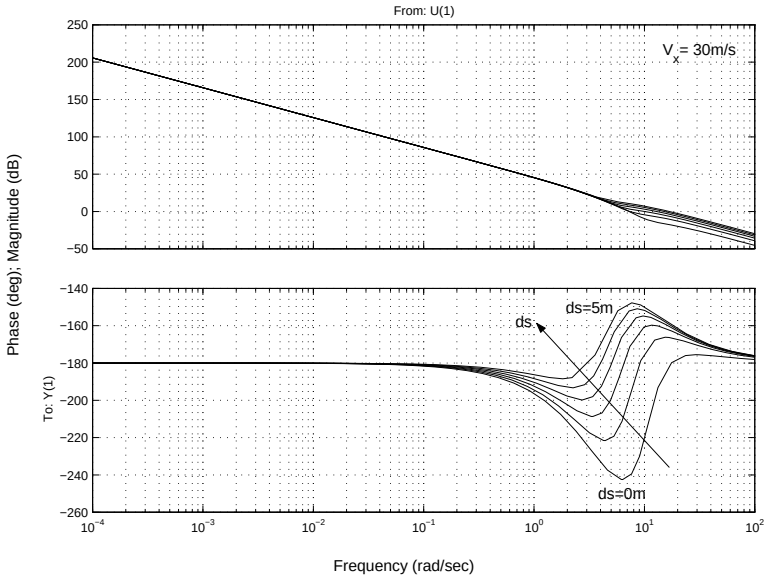

Figure 2: Bode plot of the transfer function from the steering input to the sensor output obtained at different locations)

calculated from the front and rear magnetometer measurements (denoted by y_{fs} and y_{rs} respectively) by

$$y_{vs} = \frac{(h_2 + d_s)y_{fs} + (h_1 - d_s)y_{rs}}{h_1 + h_2} \tag{21}$$

The control objective is to minimize the virtual lateral error. In other words, the control system using geometric look-ahead scheme is trying to minimize the lateral error at some distance ahead of the vehicle.

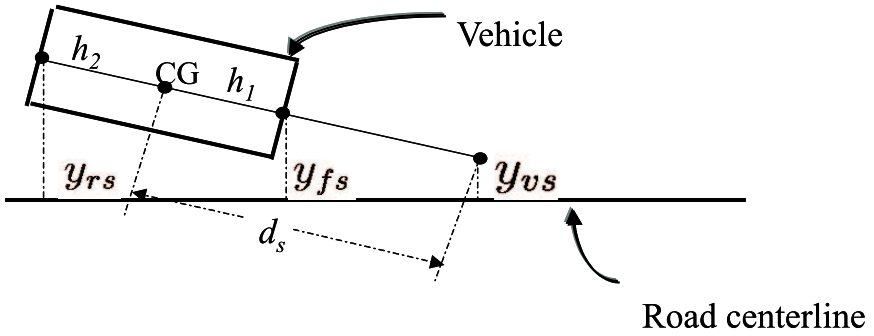

Figure 3: Geometric look-ahead scheme

In the case when one set of the magnetometers fails, the look-ahead distance in the above geometric scheme decreases to certain fixed values. This is based on the assumption that the fault detection process has been carried out and the outputs of all failed magnetometers have been set to zero. When the front magnetometers fail, only the lateral error measured by the rear magnetometers is available to the control system, and the look-ahead distance d_s decreases to $-h_2$ (h_2 is the distance from the CG to the rear bumper). Similarly, under fault in rear magnetometers, the look-ahead distance decreases to h_1 (the distance from the CG to the front bumper). In the second case, the look-ahead distance is small and the phase lead in the system may not be adequate; in the first case, the look-ahead distance is negative, and it is not even "look-ahead" any more. Figures 4 and 5 show the frequency responses from the steering input δ to the lateral error measured by the front magnetometers y_{sf} and by the rear magnetometers y_{sr} when the longitudinal velocity is $30m/s$. The decreased phase lead makes the controller design difficult, especially for the case with front magnetometer failure.

1.3 Degraded Mode Control with a Single Set of Magnetometers

With fault in either front or rear magnetometers occurs, vehicle lateral deviation is only available from the remaining set of magnetometers. In either case, d_s becomes smaller, and the luxious phase lead provided by the look-ahead scheme is no longer available. Moreover, for the Rear-Magnetometer-Based (RMB) control, the vehicle lateral dynamics has only phase lag. Closely related to the phase is the system zeros. A pair of poorly damped zeros appears when d_s is smaller (as in the case of rear magnetometer failures), and a right half plane zero appears if $d_s < -l_2$, i.e., the sensor position is actually behind the rear axle (as in the case of front magnetometer failures). More importantly, when d_s is small and fixed, the effects of the variation of the longitudinal velocity has on the vehicle lateral dynamics become more significant,

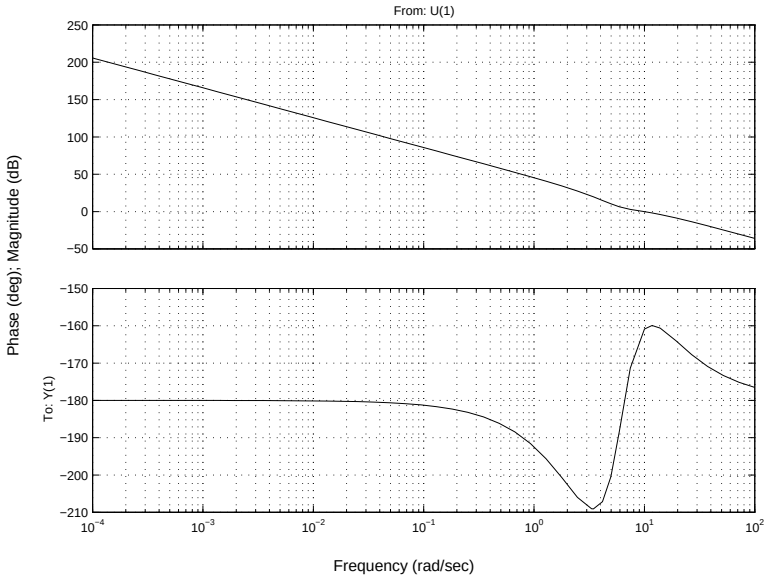

Figure 4: Bode plot of the transfer function from the steering input to front magnetometer output

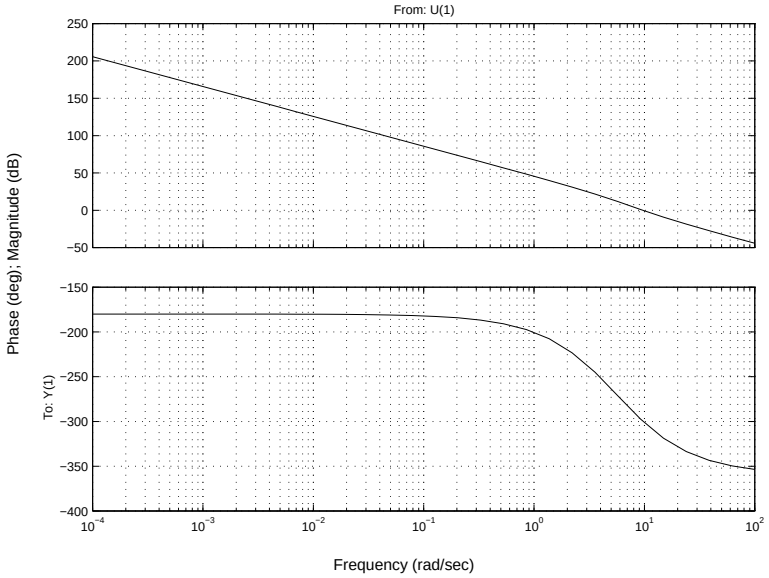

Figure 5: Bode plot of the transfer function from the steering input to rear magnetometer output

which indicates that the time varying property of the vehicle lateral dynamics can no longer be ignored. It is then doubtful that a fixed Linear Time Invariant (LTI) controller will be able to provide sufficient performance in the whole velocity operating range. This observation is also true for rear magnetometer based vehicle lateral control.

1.4 Autonomous Vehicle Following

In recent years, some researchers [10][4][5] have investigated a different approach to vehicle steering control. Instead of measuring the absolute deviation of the controlled vehicle, the on-board sensors detect the vehicle's relative position with respect to a leading vehicle, referred to as the relative deviation. The following vehicle is then controlled to follow the leading vehicle based on the relative deviation. Compared to the traditional steering control approach, this control scheme, referred to as autonomous vehicle following control, requires no road reference system. Autonomous vehicle following may work as a driver assistance system, similar to today's cruise control systems except that the system assists a driver in steering instead of speed control. It can also be combined with the cruise control system to achieve fully automated control of a vehicle.

Since the control algorithm in autonomous vehicle following is based on the vehicle's relative deviation from the leading vehicle, the lane-keeping performance of the following vehicle depends on the behavior of the leading vehicle. If the leading vehicle tracks the road centerline badly, so will the following vehicle, and in general with even worsened performance. The lead and the following vehicles now form an inter-connected system, and the tracking error of the lead vehicle is passed on to the following vehicle. This aspect of the autonomous following causes a severe string stability problem, when the algorithm is applied to a platoon of many vehicles.

String stability is concerned with propagation of tracking errors in the upstream direction of the platoon, i.e. from leading to following vehicles. A platoon may be

string unstable even if the control system of each vehicle is stable. It also places significant limitations on the performance of autonomous following control even for small groups of vehicles. This problem for autonomous following has not been analyzed in the previous research.

It is the inter-connected feature that causes the propagation of tracking errors in the platoon. To improve the vehicle tracking performance, it is intuitively helpful to weaken or cut the coupling between any two adjacent vehicles so that the tracking performance of one vehicle does not depend on that of the other. Besides the relative deviation, information on how well the preceding vehicle follows the road may also be useful for the lane-keeping control of the following vehicle. When the leading vehicle follows the road badly, the following vehicle can respond in an intelligent way and may still achieve good tracking performance. Hence, inter-vehicle communication becomes important in autonomous vehicle following control in terms of transmitting measurements of the absolute deviation of a leading vehicle to its following vehicles. Using inter-vehicle communication, a leading vehicle in the platoon, which can measure its absolute deviation (e.g. by the means of GPS, vision cameras, or magnetometers), communicates its measurements to the following vehicles. The control algorithm of a following vehicle calculates its steering input based on both the relative deviation from the leading vehicle and the communicated information to keep the vehicle in the lane.

1.5 Integrated Vehicle Control

Autonomous vehicle following control may work as a back-up system for the magnetometer-based systems when all the on-board magnetometers stop functioning. Back-up systems are also studied to deal with partial failure of the magnetometers. Currently there are two sets of magnetometers on-board each vehicle, one under the front bumper and the other under the rear bumper. Previous research indicates that the front magnetometers are critical for vehicle lateral control. More precisely, if the

front magnetometers fail, a right-half-plane zero appears on the pole-zero map of the input-output dynamics from the front wheel steering angle to the lateral error at the rear bumper, which may deteriorate the performance of the lane-keeping system. In this case, the desired vehicle performance may be achieved by combining the rear magnetometers with the autonomous vehicle following sensor. The magnetometer measurements can also help to reduce the dependence of the following vehicle on the lead vehicle, and hence reduce the tracking errors. Under this integrated control scheme, the controlled plant, i.e. the vehicle, becomes a Single Input, Two Output (SITO) system: the front wheel steering angle is the input and the rear magnetometers and LIDAR define the two outputs. In the closed-loop structure, disturbances in one system output may have strong effects on the other output. Such a problem becomes a significant concern in the design of the integrated control scheme, since the LIDAR measurements are associated with strong disturbance, which is the unknown dynamics of the leading vehicle.

1.6 Organization of the Report

This report is organized as follows. Section 2 and Section 3 illustrate the controller design using only one set of magnetometers. Section 2 describes the H_∞ optimal control with gain scheduling, and Section 3 describes the feedback linearization with a mismatched observer method. Section 4 discusses the transition behavior between the normal and degraded mode vehicle lateral control. Section 5 presents the autonomous vehicle following control algorithms. Section 6 describes the integrated controller with combined use of LIDAR and the rear magnetometers is presented. Section 7 concluds this report.

2 Vehicle Lateral Control based on H_∞ Optimal Control Techniques

Lateral control using the output of only one set of magnetometers is possible because the system is observable from the output of either the front magnetometers or the rear magnetometers. When one set of magnetometers fails, a properly designed observer can estimate all the system states based on information from the remaining set of magnetometers. Hence, the lateral error at the look-ahead distance d_s can still be calculated based on the estimated states, and then a lead-lag lateral control algorithm may be used to minimize the estimated lateral error. However, adding the observer will increase the order of the controller. Furthermore, the use of the lead-lag controller, which is designed without consideration of road curvature and sensor noise, may be problematic.

Since the system is both controllable and observable with either set of magnetometers, there should exist stabilizing output feedback controllers. Therefore, it is possible to design an output feedback controller directly, without using the look-ahead scheme. The design is based on the H_∞ optimal control theory.

2.1 Controller Design based on H_∞ Optimal Control Techniques

H_∞ optimal control techniques provide a systematic procedure for designing stabilizing output feedback controllers for controllable and observable dynamic systems. Yet the main reason for choosing H_∞ optimal control techniques in vehicle lateral control is the robustness of H_∞ controllers. The requirement for robustness arises from the variation of the vehicle lateral dynamics with the constantly changing longitudinal velocity rather than the uncertainties in system parameters. For the control system to function satisfactorily over a wide velocity range (eg. $0 \leq v \leq 40m/s$), the lateral controller has to be robust to the variation of the lateral dynamics. In the remainder

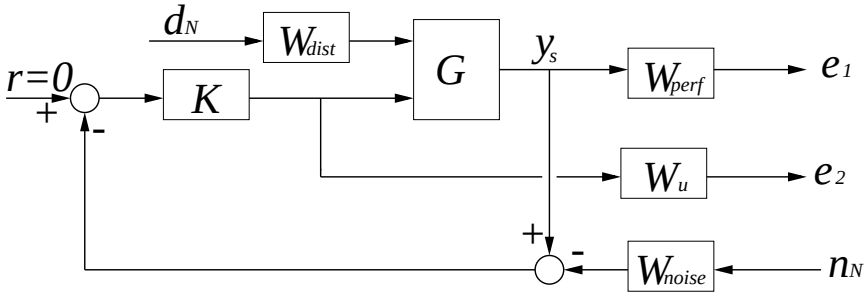

Figure 6: Formulation of H_∞ synthesis

of this section, the H_∞ synthesis for the lateral controller will be described in detail, and simulation results will be presented.

2.1.1 H_∞ Synthesis of the Lateral Controller

In the controller design based on the H_∞ optimal control theory, both the road curvature disturbance (in terms of $\dot{\epsilon}_d$, the yaw rotation rate of the road reference) and the magnetometer noise are regarded as disturbances, while the lateral error and the control effort are treated as errors. The formulation of the H_∞ synthesis for the vehicle lateral control system is shown in Figure 6. G is the bicycle model of the vehicle (Note: G for front-magnetometer based (FMB) control is different from G for rear-magnetometer based (RMB) control). W_{perf} and W_u are the weighting functions chosen according to the performance requirements on the lateral error and the limitation on the allowable control force; W_{dist} and W_{noise} model the characteristics of the disturbance $\dot{\epsilon}_d$ and the magnetometer noise. The design objective is to synthesize a controller K that minimizes the effects of the normalized disturbances (d_N and n_N) on the normalized errors (e_1 and e_2) in the sense of H_∞ norm, i.e.

$$\min \|T_{e \leftarrow d}\|_\infty \tag{22}$$

where d is $[d_N \; n_N]^T$, and e is $[e_1 \; e_2]^T$.

An important part of the H_∞ synthesis is the normalization of the disturbances

and the errors. This is also a way to specify the performance criterion and the actual disturbances. The frequency weighting functions used in these normalization are explained below.

Modeling of the lateral disturbance

The lateral disturbance $\dot{\epsilon}_d$ can be modeled from the road curvature ρ by:

$$\dot{\epsilon}_d = \rho v \tag{23}$$

where v is the longitudinal velocity. The maximum magnitude of the road curvature is set to be $1/(800m)$ in the H_∞ synthesis, which is larger than the general curvature disturbances on highways (less than $1/(1000m)$). (The larger the curvature ρ is, the sharper the curve is). Since the road curvature does not change frequently on highways, the disturbance can be modeled as a band-limited signal. Here, in order to keep the order of the controller low, the order of the disturbance model is chosen to be zero:

$$W_{dist} = \frac{v}{800} \tag{24}$$

Modeling of the magnetometer noise

Since the measurement noise generally has high frequency components, the weighting function on noise should be a high pass filter. But considering the order of the resulting controller, the noise weighting function is chosen to be a constant.

$$W_{noise} = \frac{1}{200} \tag{25}$$

Penalty on the lateral error

The high frequency component of the lateral error measurement is considered as noise. This is because the road curvature is piecewise continuous and the vehicle dynamics contains mainly low frequency dynamics. Thus the penalty is set high on the low frequency component of the lateral error measurement.

$$W_{perf} = 0.2\frac{s+30}{s+0.03} \tag{26}$$

Penalty on the steering action

The high frequency component of the control force must be restricted because it may saturate the actuator and excite the unmodeled high frequency dynamics. Therefore, the penalty is set high at high frequencies, and the bandwidth of the controller is restricted to be lower than that of the actuator (which is around 5Hz).

$$W_u = 1400\frac{s+10}{s+100} \tag{27}$$

The frequency response of the resulting controllers are shown in Figure 7 and Figure 8. From these figures, we can see that the controller using the output of the rear magnetometers alone provides more phase lead than the one using the output of the front magnetometers alone. This is as expected since the vehicle has more phase lag if the lateral error is measured at the rear bumper.

2.1.2 Simulation Results and Discussions

The designed controller has been tested in simulations. The profile of the simulated road curvature is shown in Figure 9. The road curvature changes from 0 to $-1/(800m)$ to $+1/(800m)$ and back to 0. Therefore, the maximum transition curvature is $1/(400m)$, which is much larger than the curvature on highways (less that $1/(1000m)$). The longitudinal velocity is assumed to be constant, and vehicle tracking performance at three different velocities ($20m/s$, $30m/s$, $35m/s$) are tested. The vehicle parameters remain the same as in the design. The simulations of the closed-loop system using the output of only the front magnetometers are shown in Figure 10. For the road curvature $1/(800m)$, the maximum lateral error at $v = 20m/s$ is about 5cm, and at $v = 35m/s$ is about 10cm. The steady state error is very small. Figure 11 is the simulation results of the closed-loop system using the output of only

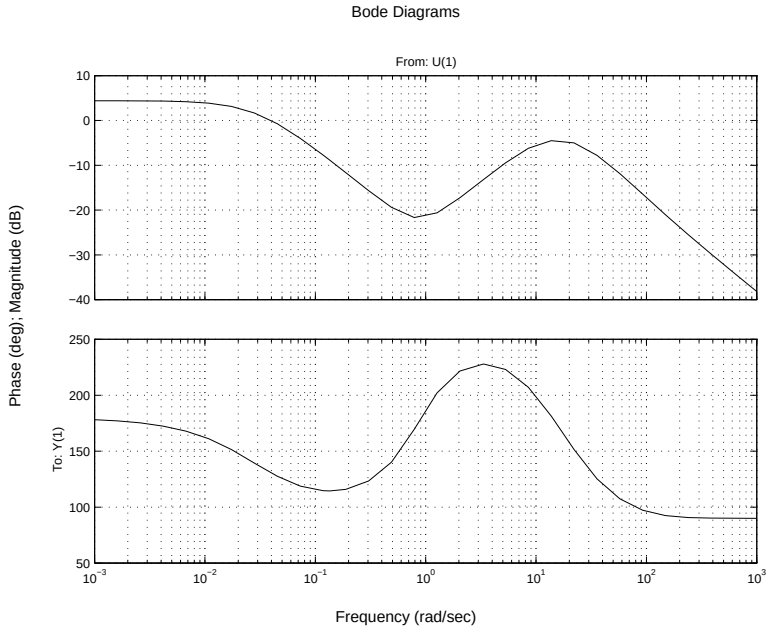

Figure 7: Bode plot of the controller with front magnetometers

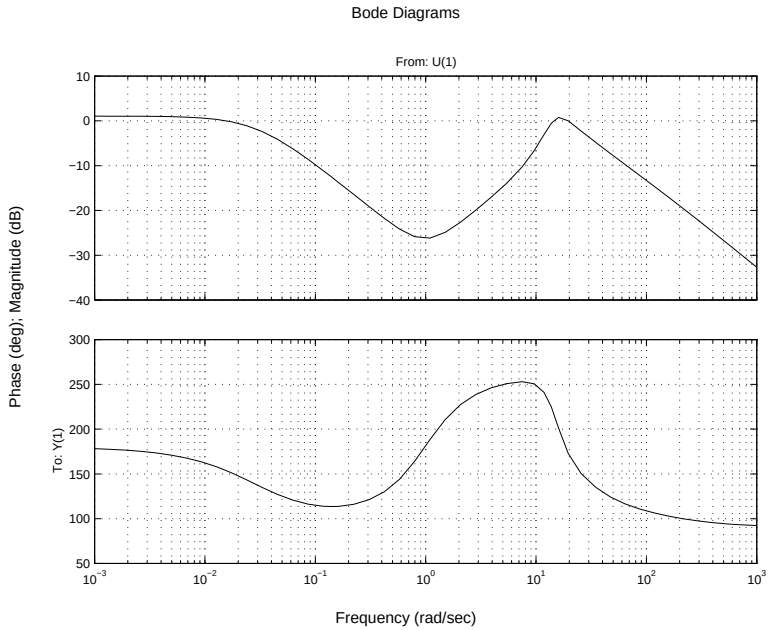

Figure 8: Bode plot of the controller with rear magnetometers

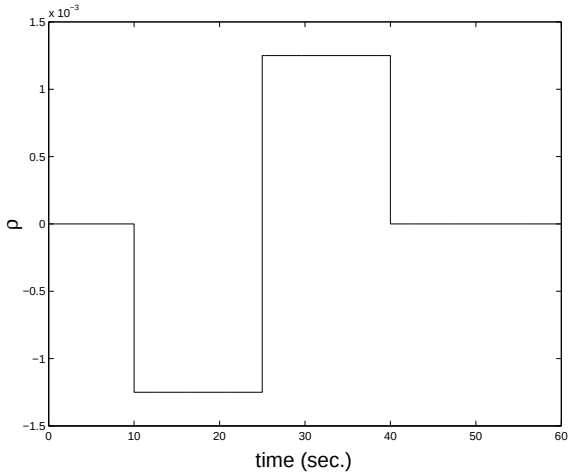

Figure 9: Profile of the road curvature used in the simulations

the rear magnetometers. The lateral error for road curvature $1/(800m)$ at $v = 20m/s$ is about 10cm, which is larger than the error with front magnetometers, but much smaller than the allowable error (at road curvature transition from 0 to $1/(1000m)$, the maximum error should be less than 30cm). However, the oscillations are so severe at $v = 35m/s$ that the controller must be fine tuned or redesigned to achieve smooth riding.

Further analysis reveals where these oscillations come from. For FMB control, it is observed that as the longitudinal velocity gets higher, the system zeroes in the transfer function from the tire steering angle to the front magnetometer output become more weakly damped. Hence the fixed H_∞ controller results in worse locations for the closed-loop poles at higher velocities. Similarly, for RMB control, a RHP zero appears in the transfer function from the steering angle to the rear magnetometer output. As velocity increases, the RHP zero moves further away from the origin, and the fixed H_∞ controller draws the closed-loop poles closer to the imaginary axis. Both cases render weakly damped poles in the closed-loop system, and lead to more severe oscillations in the time domain response. To subdue the oscillation, smaller feedback gain is prefered at higher velocities. However, with a fixed controller, this will definitely induce larger lateral errors, especially at low velocities where the gain

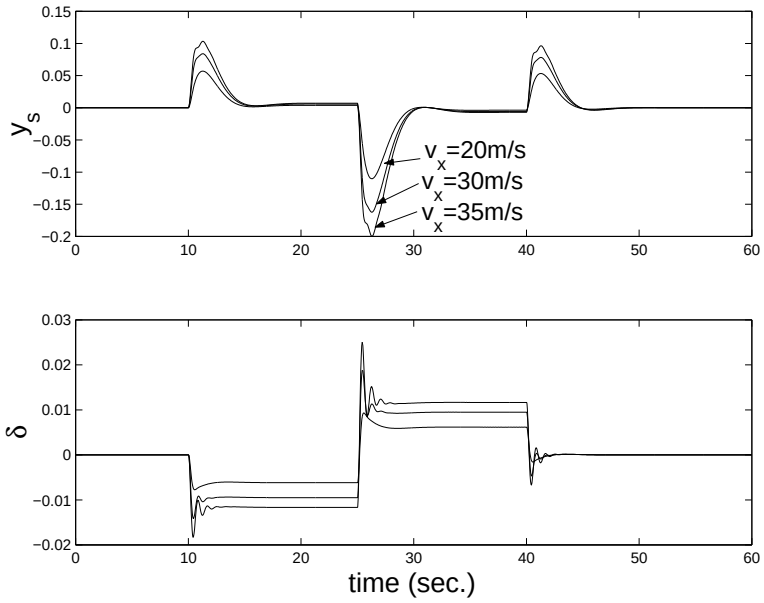

Figure 10: Simulation of the controller with front magnetometers

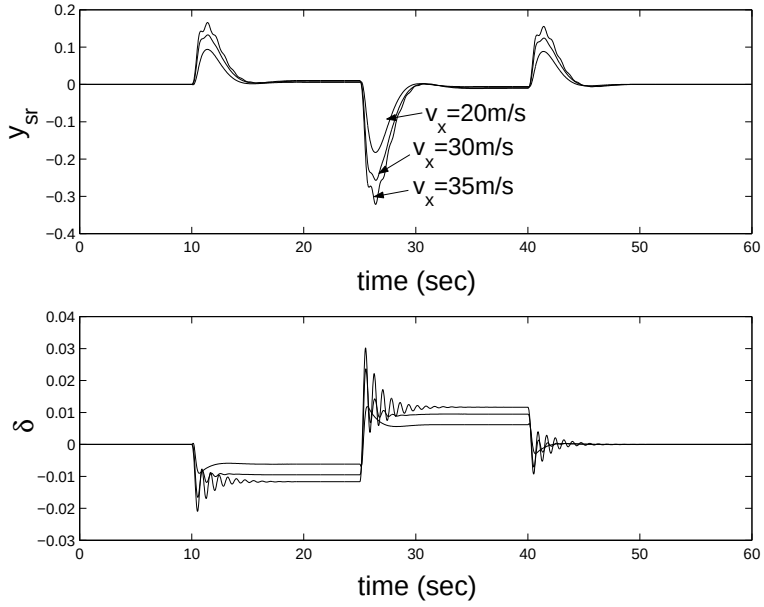

Figure 11: Simulation of the controller with rear magnetometers

of the vehicle lateral dynamics itself is small. Hence, with a fixed lateral controller, the design will struggle for a balance between small lateral errors and comfortable riding without any noticeable oscillations.

It is important to realize that this tradeoff is much more difficult provided that only one fixed controller is employed. Without this constraint, it will be easier to meet the requirements for both high velocity and low velocity lateral control. The reason lies in the following two observations: (1)At high velocities the gain of the vehicle lateral dynamics is much higher than that at low velocities; therefore, the controller gain for high velocity lateral control can be lowered for the same tracking accuracy; (2)The controller gain is allowed to be higher at low velocities since the zeroes are more damped at low velocities. Hence low velocity lateral control and high velocity lateral control actually pose different challenges, and they indeed demand different controllers for optimal results.

2.2 Gain Scheduled H_∞ controller

As mentioned in the last section that the H_∞ control techniques are applied to reduce the effects of the longitudinal velocity variation on the lateral dynamics. However, the simulations show that even though the controller can maintain small lateral errors in a wide range of longitudinal velocities, oscillations become more severe as the velocity deviates further away from the nominal velocity used in the H_∞ synthesis. These oscillations greatly aggravate the riding comfort, and must be eliminated. Further discussion in Section 2.1.2 indicates that fine tuning of the controller will help, but only to a limited extent. To abtain small lateral error and good riding comfort over a wide operating range, gain scheduling is then introduced.

Four H_∞ controllers are designed by fixing the longitudinal velocity at $10m/s$, $20m/s$, $30m/s$ and $40m/s$. The weighting functions remain the same as those used in the single H_∞ controller design. The front-magnetometer based controllers are shown in Figure 12. Here, we see that the main difference is the phase at around

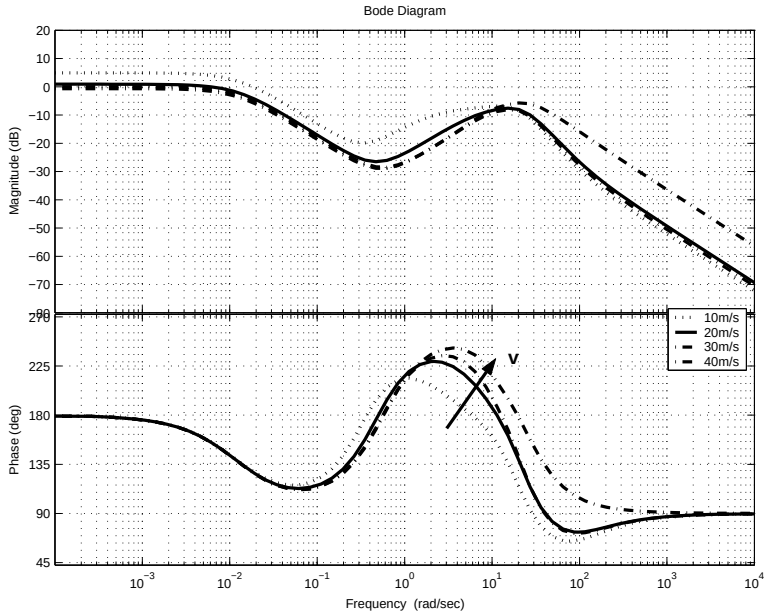

Figure 12: Bode plot of the front controllers designed at velocity $10m/s$, $20m/s$, $30m/s$ and $40m/s$

$1 - 10rad/sec$, i.e., the controllers designed at higher velocities provide more phase lead in order to compensate for the increasing phase lag of the vehicle lateral dynamics. Meanwhile, the low frequency gain of the controllers at higher velocities also decreases, which compensates for the increase in the low frequency gain of the vehicle lateral dynamics. Moreover, the decrease in the low frequency gain contributes to prevent the closed-loop poles from getting too close to the more weakly damped zeros at higher velocities, which in term helps to avoid severe oscillations and maintain good riding quality. However, the gain decrease also results in larger lateral error at higher velocities as shown in the simulation results (Figure 13). The simulations are conducted with the same settings given by Table 1. No observable oscillation appears in the simulation results, though the largest lateral error is almost $0.3m$ (maximum lateral error allowed) at $v = 40m/s$.

Similarly, the rear-magnetometer based gain scheduled controller has been designed (Figure 14). Again, the controllers designed at higher velocities provide larger

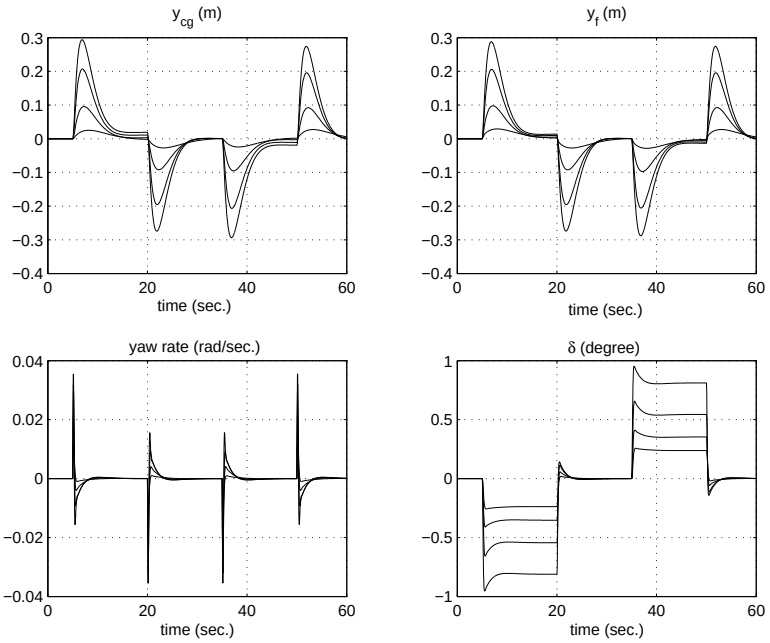

Figure 13: Simulation of the gain scheduled controllers with front magnetometers

phase lead at around $1 - 10 rad/sec$. The low frequency gain of the controllers does not differ much, which may be due to the fact that the limitation posed by larger RHP zeros is actually milder. The simulation results with this gain scheduled controller is shown in Figure 15.

2.3 Summary

This section has described the degraded mode lateral controller design based on the H_∞ optimal control theory. With fault in either front or rear magnetometers, the degraded mode control has been reconfigurated with the remaining set of magnetometers. By including the road curvature and the sensor noise as disturbances, the derived controllers are optimal in the sense of minimizing the effect of the road curvature and the sensor noise on the lateral error and the control force. Two controllers have been designed, one using only the output of the front magnetometers, the other using only output of the rear magnetometers. Simulations have shown that the lat-

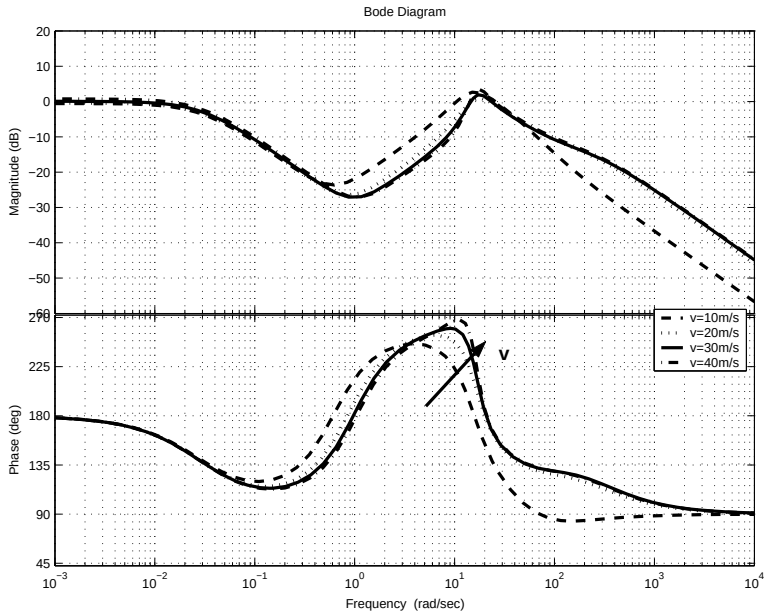

Figure 14: Bode plot of the rear controllers designed at velocity $10m/s$, $20m/s$, $30m/s$ and $40m/s$

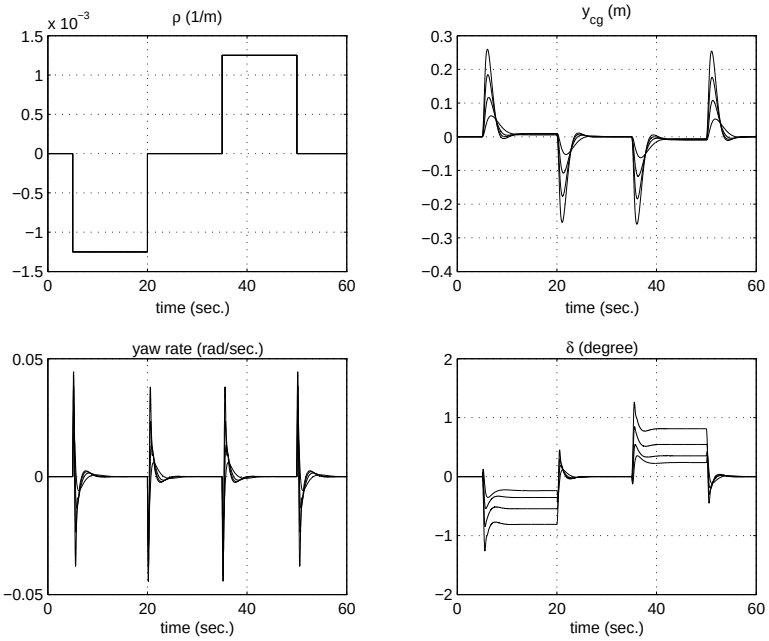

Figure 15: Simulation of the gain scheduled controllers with rear magnetometers

eral error is within the acceptable range, yet severe oscillations occur at the velocities higher than $30m/s$. To maintain both small lateral errors and good riding comfort, gain scheduling has been introduced to achieve satisfactory performance over a wide range of velocity. Four different H_∞ controllers have been designed at $10m/s$, $20m/s$, $30m/s$ and $40m/s$ respectively. The simulation results have shown adequate tracking performance of these controllers.

3 Vehicle Lateral Control based on Feedback Linearization with Mismatched Observer

In Section 2, H_∞ control techiniques have been employed to design a Linear Time Invariant (LTI) controller in the hope that the variation of the vehicle lateral dynamics can be handled by the robustness of the H_∞ controller. Nevertheless, simulations and further discussions indicate that a fixed controller will not be able to provide adequate performance in the whole operating range (i.e. $0 < v \leq 40m/s$). Therefore, several LTI controllers were designed, each designed at a specific nominal velocity, and the control force is switched among these controllers according to the actual longitudinal velocity. Simulations in Section 2 show that this gain-scheduling method works well. However, this method may not be amenable to stability analysis, easiness of implementation and performance optimization.

In this section, the control problem is tackled from a different perspective. Instead of fixing the longitudinal velocity to make the lateral dynamics Linear Time Invariant (LTI), the vehicle lateral dynamics is now treated as Linear Time Varying (LTV) and the controller design targets at the time varying property directly rather than employing gain scheduling later on. Since the front-magnetometer-based vehicle lateral dynamics has weakly damped zeros, the degraded mode lateral control based on front magnetometer output can be casted as the control of a LTV plant with weakly damped zeros. Similarly, the rear-magnetometer-based lateral control can be casted

as the control of a LTV plant with a nonminimum phase zero.

Popular control methods for LTV plants include the gain scheduling control and Linear Parameter Varying (LPV) control. The LPV control technique has been developed for LPV systems, a specific kind of LTV systems whose system matrices are functions of some varying parameters. The designed LPV controller also has system matrices which are functions of the same varying parameters. In practice, solutions are found by griding the varying parameters and LTI controllers are constructed from these solutions. As a consequence, the controller still involves switching or linear interpolation between these LTI controllers [8].

In this Section, a simple LTV controller without any switching mechanism is sought after. The design method is based on feedback linearization with mismatched observer. This approach is first applied to the front-magnetometer-based (FMB) control where the vehicle lateral dynamics has weakly damped zeros. First, the design procedure is described in detail. Later on, the approach is utilized to design the rear-magnetometer-based (RMB) control, where the vehicle lateral dynamcs has one nonminimum phase zero. Experimental results are included to demonstrate the effectiveness of the design.

3.1 LTV controller design based on Feedback Linearization with Mismatched Observer

3.1.1 Basic Ideas

Feedback linearization has been recognized as a powerful method for nonlinear or time varying systems. Hence, it is natural to apply feedback linearization to LTV systems to cancel out the time varying terms and function as gain scheduling. Since it is generally impractical to have all the states measured for feedback control, observers are normally used to obtain state estimates for feedback linearization. Widely used linear observers such as the Luenberger observer and Kalman filter are matched

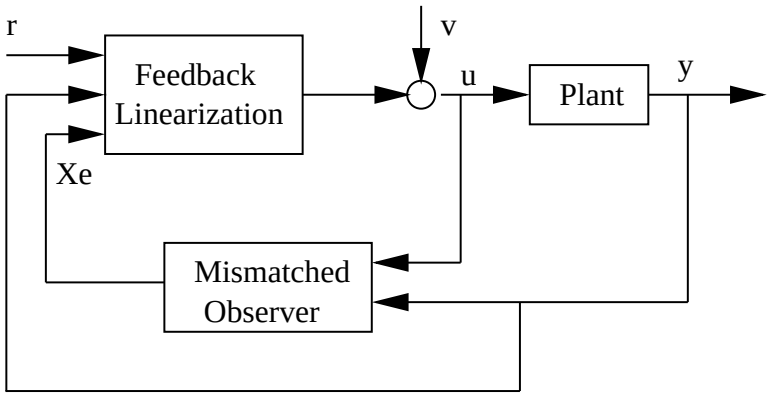

Figure 16: Closed-loop configuration with the mismatched observer

observers, i.e., the observer has exactly the same structure and coefficients as the plant with an extra term of the output measurement for correction. If the relative degree is not zero, internal dynamics will result from feedback linarization. If matched observers are used to estimate the states, the open-loop zeros of the plant will be contained as the closed-loop poles of the internal dynamics. Moreover, since the front-magnetometer-based (FMB) vehicle lateral dynamics has weakly damped zeros and the rear-magnetometer-based (RMB) vehicle lateral dynamics has a RHP zero, with the feedback of either the states or the state estimates from the matched observer, the internal dynamics will become weakly damped for the FMB control or unstable for the RMB control.

There are two possible ways to solve this problem: one is to eliminate the internal dynamics and the other is not to use matched observers for state estimation. The former way can be achieved by choosing an output such that the relative degree is zero; however, this is not practical in our case due to the limitation of sensor choices. The latter way is to design an observer that can provide fairly accurate state estimates without leaving the open-loop zeros as the internal dynamics modes. Such an observer should not be matched, otherwise, the open-loop zeros will be trapped in the internal dynamics. In other words, the structure of this mismatched observer does not directly depend on the plant any more. Figure 16 shows the overall closed-

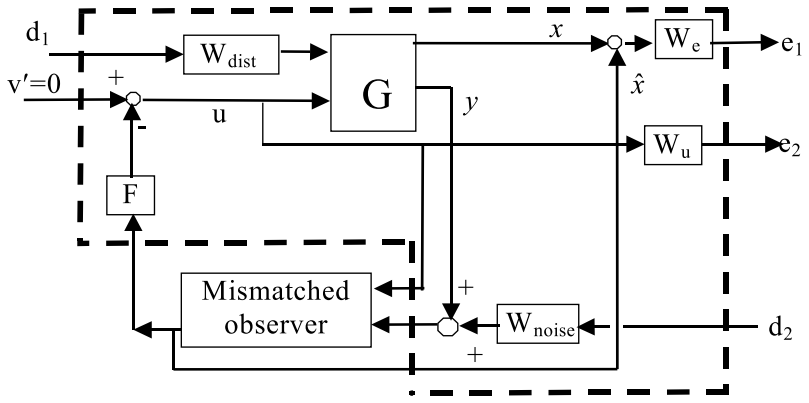

Figure 17: The H_∞ synthesis of the mismatched observer

loop configuration of feedback linearization with mismatched observer. The goal of using the observer is to generate fast and well-damped closed-loop modes as well as to estimate the states accurately. It may be true that such a mismatched observer will not be able to provide state estimates as accurately as those matched observers, which is a sacrifice made for better closed-loop modes. The mismatched observer has two competing objectives: to provide accurate state estimates for feedback linearization and to render the overall closed-loop system well-damped. The design of this observer has to balance between these two objectives. Moreover, now that the structure of this observer is not restricted, there is more freedom in its design. Due to the multiple objectives and the Multi-input Multi-output (MIMO) nature of the observer, H_∞ optimal control techiniques are employed in the design. Since one main objective of the observer is to estimate the states accurately, the H_∞ synthesis is formulated to minimize the H_∞ norm of the transfer function from the lateral disturbance and sensor noises to the estimation errors. To avoid actuator saturation and excitation of high frequency modes, a weighting function on the control input is also included. The overall closed-loop behavior is shaped by appropriate weighting functions. Figure 17 shows the H_∞ synthesis for the design of the mismatched observer.

3.1.2 The FMB Controller Design based on Feedback Linearization with Mismatched Observer

In this section, the front-magnetometer-based (FMB) vehicle lateral control is to be designed. Thus, the lateral output referred in this section is always y_f.

The relative degree of the vehicle lateral dynamics is 2; therefore, the desired closed-loop system is of 2nd order, and it can be written as:

$$\ddot{y}_f + k_1\dot{y}_f + k_2 y_f = \ddot{y}_d + k_1\dot{y}_d + k_2 y_d \tag{28}$$

where y_d is the desired value for y_f (the lateral error at the front bumper). Since it is a regulation problem, $\ddot{y}_d = \dot{y}_d = y_d = 0$. Based on the desired closed-loop dynamics and vehicle model (Eq. 9), the control input can be easily derived:

$$\delta = \frac{-k_1\dot{y}_f - k_2 y_f - (A_2 + d_1 A_4)\hat{X}}{b_{21} + d_1 b_{41}} \tag{29}$$

where A_2 and A_4 are the second and fourth rows of A matrix in the state equations (Eq. 9), and $\hat{X}$ is the state estimates given by the mismatched observer. d_1 is the distance from the front bumper to the vehicle mass center, and b_{21} and b_{41} are elements in B matrix (Eq. 9). Note that the feedback gain is a function of the system matrix A that varies with the longitudinal velocity; therefore, the feedback gain also varies with the longitudinal velocity.

The H_∞ synthesis is shown in Figure 17. Both the road curvature and the sensor noise are regarded as disturbances; and in order to provide accurate estimates for feedback linearization, the difference between the states and their estimates is treated as an error to be minimized. The control force u is also penalized to avoid actuator satuation and excitation of high frequency modes.

The weighting functions on the lateral disturbance $\dot{\epsilon}_d$, magnetometer noises, and the control input are the same as those used in Section 2. Additionally, there should be four weighting functions for the estimation errors, since there are four states to estimate. The weighting function on the estimation error of x_1, the lateral deviation

at vehicle's CG, is to meet similar requirement as those for the weighting on the lateral error y_f. The high frequency component of the lateral error measurement is considered as noise. This is because the road curvature is piecewise continuous and the vehicle exhibits mainly low frequency dynamics. Thus the penalty is set high at low frequencies.

$$W_{x_1} = 50\frac{s+0.2}{s+0.1} \tag{30}$$

The weightings on the estimation errors of the lateral deviation derivative and the yaw rate are set to 1. Noticing that $y_f = x_1 + d_1 x_3$, the weighting on the yaw angle x_3 is set to be $d_1 W_{x_1}$. Hence the weighting function on the estimation error vector is:

$$W_e = \begin{bmatrix} W_{x_1} & 0 & 0 & 0 \\ 0 & 1 & 0 & 0 \\ 0 & 0 & d_1 W_{x_1} & 0 \\ 0 & 0 & 0 & 1 \end{bmatrix} \tag{31}$$

The resulting controller is the combination of feedback linearization and the mismatched observer. Note that while the feedback gain changes with the longitudinal velocity, the mismatched observer is fixed. Hence the implementation of the controller is much simpler than general gain scheduled controllers. Figure 18 shows the frequency response of the resulting controller at four different longitudinal velocities. As the longitudinal velocity increases, the controller provides a larger phase lead to compensate the increasing phase lag of the vehicle lateral dynamics.

3.1.3 Experimental Results

Experiments have been conducted at the Richmond Field Station of the University of California, Berkeley. The testing vehicle is a Buick LeSabre car. Its parameters are shown in Table 1. The controller after fine tuning is shown in Figure 19. The main difference between the original design (Figure 18) and the fine-tuned design (Figure 19 is in the low frequency gain. After fine tuning, the controller has achieved

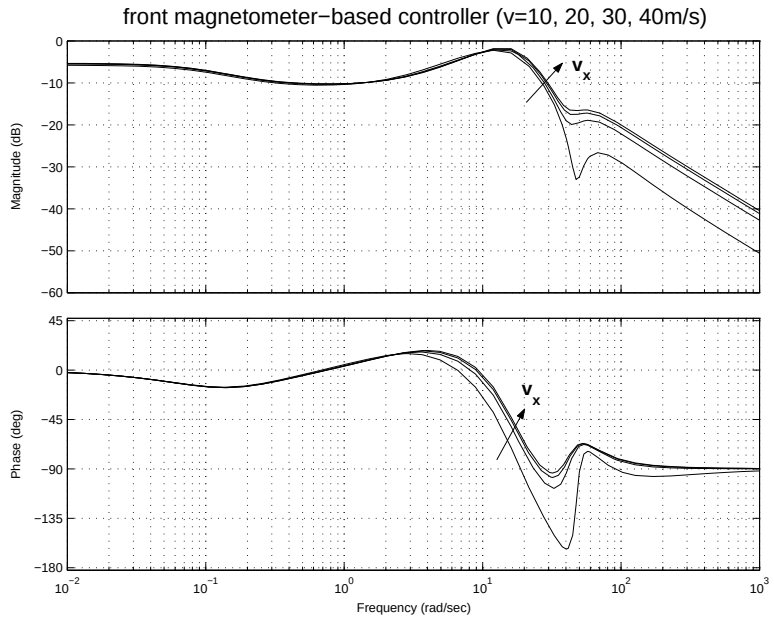

Figure 18: Frequency response of the controller based on feedback linearizatio and mismatched observer

the performance shown in Figure 20. ρ is the road curvature of the test track at the Richmond Field Station. Here, the largest and smallest radii of the curve are about $480m$ and $220m$; they are significantly smaller than the radii of general highway curves, which are larger than $1000m$. y_f and y_r are the measurements of front magnetometers and rear magnetometers. For longitudinal velocity up to $16m/s$, the maximum lateral error is about $0.1m$ (the lateral error at the beginning depends on the initial position of the vehicle relative to the road centerline, and it should not be regarded as the controlled lateral error). The steady state lateral error on a straight lane is smaller than $0.02m$. Figure 20 shows that the steering input δ is smooth, with the frequency component at about $1Hz$.

The vehicle was tested up to $20m/s$ at the Richmond Field Station (only low speed testing is allowed at the Richmond Field Station), and the performance was quite satisfactory in this speed range.

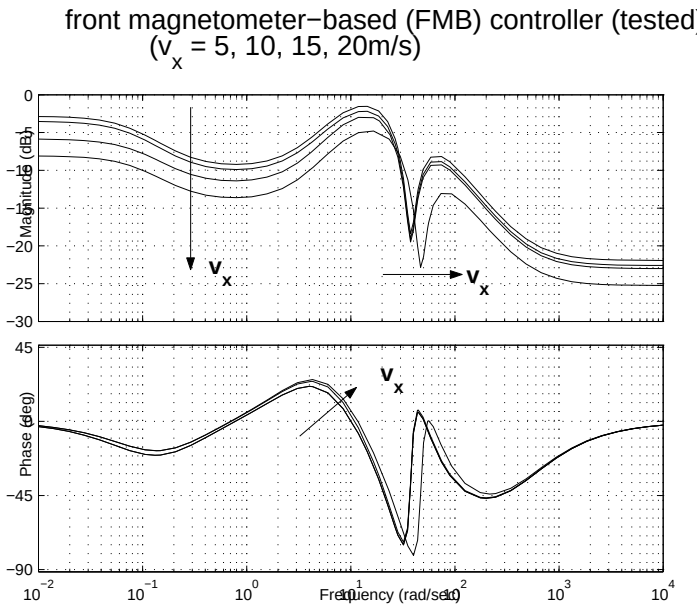

Figure 19: Frequency response of the controllers tested in experiments

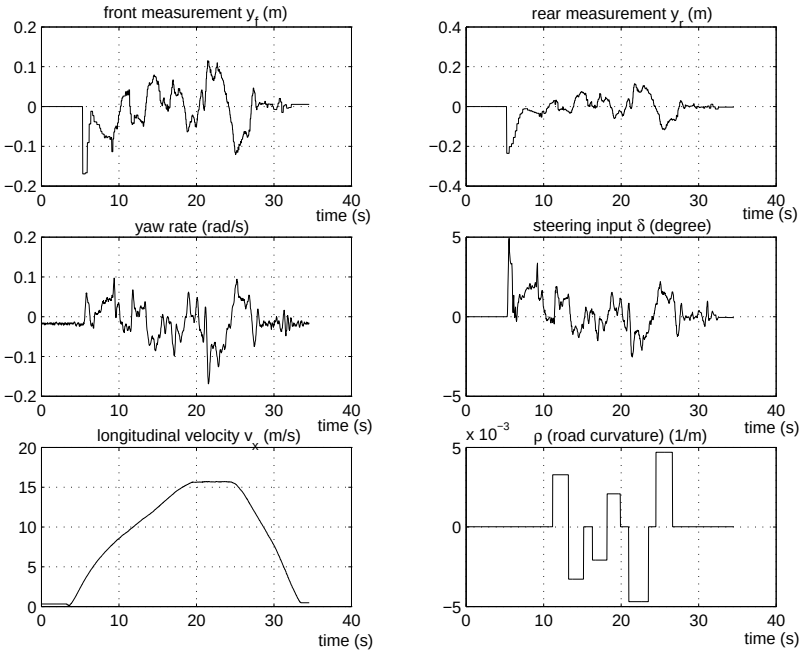

Figure 20: The experimental result (testing vehicle: Buick Lesabre)

3.2 Discussion on Stability

At first glance, one may take it for granted that the closed-loop system will be stable because of the use of H_∞ optimal control techniques. However, even with exact state feedback, feedback linearization only results in a LTI input-output relationship. In other words, time-varying terms still exist in the vehicle lateral dynamics, but they do not appear in the input-output relationship. Therefore, to design the mismatched observer based on H_∞ techniques, the vehicle lateral dynamics should still be fixed (in the case here, the velocity is fixed to be $20m/s$ for the observer design). Consequently, the H_∞ techniques will only guarantee closed-loop stability at this specific velocity (i.e. $v = 20m/s$); there is no guarantee for stability in the whole operating range ($0 \leq v \leq 40m/s$).

To analyze the stability in the whole operating range, the concept of Quadratic Stability (QS) is utilized. According to [14], define the Linear Parameter Varying (LPV) systems and the Quadratic Stability of LPV systems as follows:

Definition 4.2.1 *Linear Parameter Varying (LPV) System*
Assume that the following are given:

- *a compact set* $\mathcal{P} \subset R^s$,
- *a function* $A \in \mathcal{C}^0(R^s, R^{n\times n})$,
- *a function* $B \in \mathcal{C}^0(R^s, R^{n\times n_d})$,
- *a function* $C \in \mathcal{C}^0(R^s, R^{n_e\times n})$, *and*
- *a function* $D \in \mathcal{C}^0(R^s, R^{n_e\times n_d})$.

where R^n *denotes a set of n-dimentional real vectors,* $R^{n\times m}$ *a set of n-by-m matrix with elements all real numbers, and* $\mathcal{C}^0(U, V)$ *a set of continuous functions from* U *to* V.

An n-th order linear parameter varying (LPV) system is the one whose dynamics

evolves as:

$$\begin{bmatrix} \dot{x}(t) \\ e(t) \end{bmatrix} = \begin{bmatrix} A(\rho(t)) & B(\rho(t)) \\ C(\rho(t)) & D(\rho(t)) \end{bmatrix} \begin{bmatrix} x(t) \\ d(t) \end{bmatrix} \tag{32}$$

where $\rho \in \mathcal{F}_{\mathcal{P}}$, $x(t)$, $\dot{x}(t) \in R^n$, $d(t) \in R^{n_d}$ *and* $e(t) \in R^{n_e}$

Note: As the matrix functions A, B, C and D are continuous functions of the parameter ρ, they are, in fact, norm-bounded on the compact set $\mathcal{P}$.

$\mathcal{F}_{\mathcal{P}}$ is the parameter variation set defined as follows:

Definition 4.2.2 *Parameter Variation Set*

Given a compact set $\mathcal{P} \subset R^s$*, the parameter variation set* $\mathcal{F}_{\mathcal{P}}$ *denotes the set of all piecewise continuous functions mapping* R^+ *(eg. time t) into* $\mathcal{P}$ *with a finite number of discontinuities in any interval.*

Note: The notation $\rho \in \mathcal{F}_{\mathcal{P}}$ denotes a time-varying trajectory in the parameter variation set, while $\rho \in \mathcal{P}$ denotes a vector in a compact subset of R^s.

We now define the Quadratic Stability for LPV systems.

Definition 4.2.3 *Quadratic Stability*

Given a compact set $\mathcal{P} \subset R^s$*, and a function* $A \in \mathcal{C}^0(R^s, R^{n \times n})$*, the function A is quadratically stable over* $\mathcal{P}$ *if there exists a matrix* $P \in S_+^{n \times n}$*, such that for all* $\rho \in \mathcal{P}$

$$A^T(\rho)P + PA(\rho) < 0 \tag{33}$$

with $S_+^{n \times n}$ *a set of n-by-n positive definite matrices.*

Quadratic Stability ([1], [14]) is a strong notion of robust stability in the sense that it holds for arbitrarily fast variation in the parameter trajectory ρ, and its definition involves a single quadratic Lyapunov function.

Definition 4.2.4 *Quadratic Stability of LPV systems*

Given a LPV system defined in Definition 4.2.1, if A is quadratically stable over $\mathcal{P}$*, then the system is a quadratically stable LPV system.*

We may also define the exponential stability for LPV systems as follows:

Definition 4.2.5 *Exponential Stability*

The LPV system in Definition 4.2.1 is exponentially stable if there exist some con-

stants M, $\alpha > 0$, such that for all $\rho \in \mathcal{F}_{\mathcal{P}}$ and all $t \geq \tau$

$$\|\Phi_\rho(t,\tau)\| \leq Me^{[\alpha(t-\tau)]} \tag{34}$$

It is well known that for LTI systems, Quadratic Stability is equivalent to Exponential Stability [13]. But for LPV systems, these two concepts are not the same any more. Actually, the Quadratic Stability implies Exponential Stability [14]. Hence, Quadratic Stability is a strong stability concept for LPV systems. Furthermore, its definition also provides a method to prove or verify the stability of a LPV system.

One confusion to be clearified is that the criterion for quadratic stability (Eq. 33) differs from the condition that $A(\rho)$ matrix is Hurwitz over the set $\mathcal{P}$. $A(\rho)$ being Quadratically Stable certainly implies that $A(\rho)$ is Hurwitz over the set $\mathcal{P}$, but it is possible that there does NOT exist a P matrix satisfying Eq. 33 for an $A(\rho)$ matrix that is Hurwitz over the set $\mathcal{P}$. In other words, $A(\rho)$ being Quadratically Stable is stronger than $A(\rho)$ being Hurwitz over the same $\mathcal{P}$.

In the vehicle lateral control problem, the corresponding varying parameter is the longitudinal velocity v, and the set $\mathcal{P}$ is $\{v : \epsilon \leq v \leq 40\}$ with ϵ a small number, say 0.01, such that the set $\mathcal{P}$ is compact and the system matrices of the vehicle lateral dynamics has definition over $\mathcal{P}$. To verify that the closed-loop system is indeed quadratically stable, we need to show that the closed-loop system is a LPV system, and then to prove that its system matrix $A_{clp}(v(t))$ is quadratically stable.

Vehicle lateral dynamics presented in Section 1 can be represented as:

$$\begin{aligned} \dot{X} &= A(v)X + B\delta + W(v)\dot{\epsilon}_d \\ y_f &= C_f X \end{aligned} \tag{35}$$

where the matrices $A(v)$ and $W(v)$ are functions of the longitudinal velocity v, and the matrices B and C_f are actually independent of v. With the feedback linearization: $\delta = F(v)\hat{X}$, and the fixed observer:

$$\dot{\hat{X}} = A_o\hat{X} + B_{o1}\delta + B_{o2}y_f \tag{36}$$

where the matrixes A_o, B_{o1} and B_{o2} are all fixed, the closed-loop A matrix can be derived as:

$$A_{clp}(v) = \begin{bmatrix} A(v) & BF(v) \\ B_{o2}C_f & A_o + B_{o1}F(v) \end{bmatrix} \tag{37}$$

To prove the closed-loop system is quadratically stable, the Linear Matrix In equality (LMI)

$$A_{clp}^T(v)P + PA_{clp}(v) < 0, \quad over\ \epsilon \leq v \leq 40m/s \tag{38}$$

must be solved for $P \in S_+^{n\times n}$, where ϵ is set to a very small number such that the compact set $\epsilon \leq v \leq 40m/s$ can represent the operating range $0 < v \leq 40m/s$. Here, choose $\epsilon = 0.01$. Notice that Equation (38) is an affine function of P and it is in the form of Linear Matrix Inequality (LMI), which has advantages for solving P from a computational view. By finding a positive definite P, the closed-loop control system can be proved quadratically stable.

3.3 RMB Control based on Feedback Linearization and Mismatched Observers

Now same idea is applied to the rear-magnetometer-based (RMB) vehicle lateral control. With the same desired closed loop dynamics (Eq. 28) and the same weighting functions in the design of the mismatched observer for the FMB controller, a LTV controller for the RMB control can be derived. However, the resulting controller has two problems. One is that even at the velocity it is designed for, the perfomance is not quite satisfactory. Simulation results show observable oscillations and the oscillation mode matches the mode in the yaw dynamics. The other is that this LTV controller can no longer achieve quadratic stability. The first observation indicates that the weighting functions in the H_∞ synthesis are not appropriate for the RMB controller design. For different plants to achieve the same required performance, the controller must be different and the more different the plants the more different the controllers. In H_∞ design, the controller characteristics depend on the weighting functions at

both low and high frequencies and the H_∞ synthesis provides better robustness by fine tuning the controller characteristics at around the crossover frequency. The difference between the FMB and RMB vehicle lateral dynamics is significant in both the low frequency gain and the phase, and the weighting functions suitable for the FMB controller design are no longer suitable for the RMB controller design. According to the RMB vehicle lateral dynamcis, the same weighting function for the disturbances (road curvature and sensor noise) and the control input are used. The gain of the weighting function on the estimation error of the lateral deviation is lowered to allow more freedom in phase:

$$W_{x_1} = 30\frac{s+0.2}{s+0.1} \tag{39}$$

$$W_e = \begin{bmatrix} W_{x_1} & 0 & 0 & 0 \\ 0 & 1 & 0 & 0 \\ 0 & 0 & d_1 W_{x_1} & 0 \\ 0 & 0 & 0 & 1 \end{bmatrix} \tag{40}$$

The redesigned controller provides satisfactory performance at the specific velocity it is designed for. As discussed in Section 3.2, the designed mismatched observer will achieve stability only at the specific velocity it has been designed and QS can be used to examine whether or not the overall system is stable in the operating range. Unfortunately, in the case of RMB control, the designed mismatched observer can not achieve QS in the operating range. The main reason comes from the time-varying RHP zero in the RMB vehicle lateral dynamics.

One way to ensure QS with a single mismatched observer is to formulate the observer design into a convex optimization problem by incorporating the QS requirement in the design. As in Section 3.2, with the feedback linearization, $\delta = F(v)\hat{X}$, and the fixed observer (Eq. 36), the closed-loop A matrix is:

$$A_{clp}(v) = \begin{bmatrix} A(v) & BF(v) \\ B_{o2}C_f & A_o + B_{o1}F(v) \end{bmatrix} \tag{41}$$

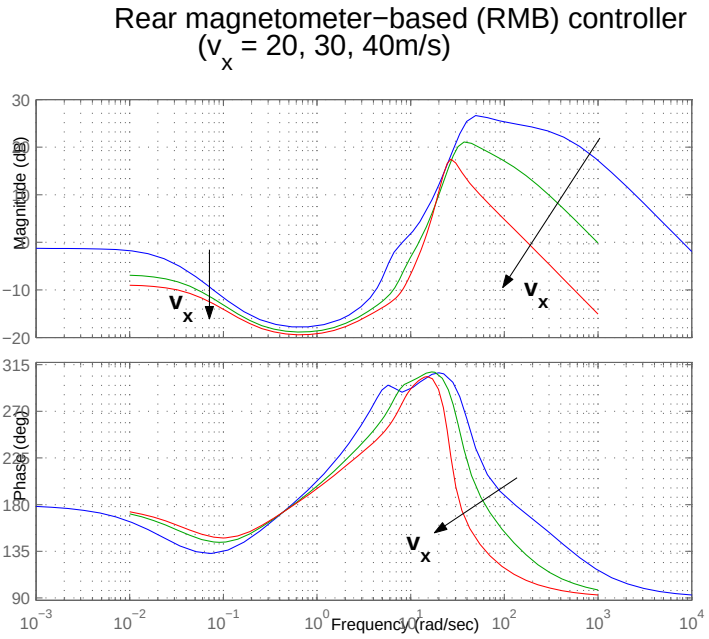

Figure 21: The RMB controllers

where the matrices A_o, B_{o1} and B_{o2} are the system matrices of the observer and are all fixed. The design problem is to solve for A_o, B_{o1} and B_{o2} such that there exists a $P \in S_+^{2n\times 2n}$ that satisfies $A_{clp}^T(v)P + PA_{clp}(v) < 0$ for $\epsilon \leq v \leq 40m/s$ ($\epsilon = 0.01$). This can be casted and solved as a convex optimization problem [9].

In this report, instead of solving a convex optimization problem, several mismatched observers are designed at different longitudinal velocities, and they are gain scheduled. Figure 21 shows the characteristics of the RMB controllers at $v = 20, 30, 40m/s$, each consists of the mismatched observer designed at the corresponding velocity and the time varying state feedback. Low speed testing has been conducted at the Richmond Field Station with the same Buick LeSabre Car. Figure 22 shows the experimental results. The maximum lateral error is about 0.1m. Again, the steering input δ is smooth and is similar to human driving. No noticeable oscillation occurs.

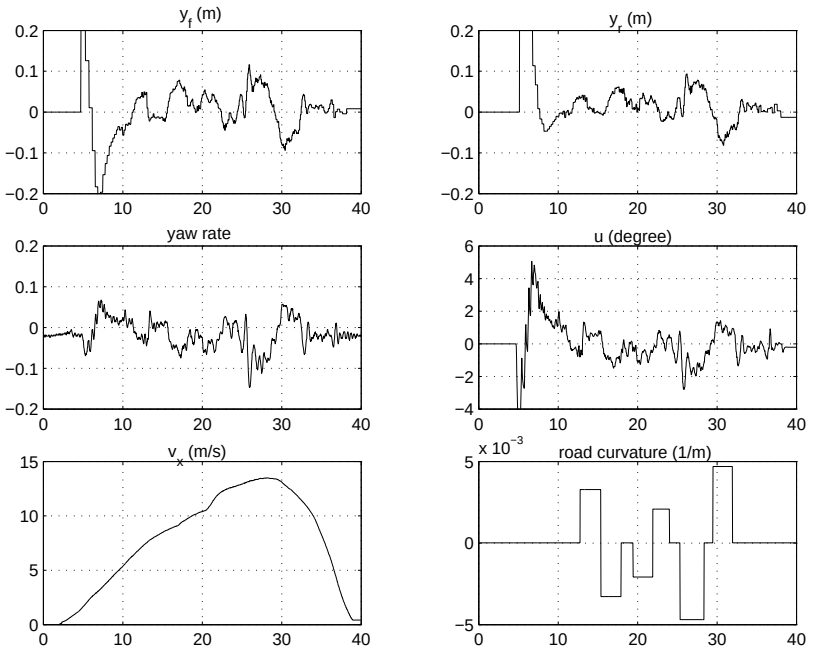

Figure 22: The experimental result with the RMB controllers (testing vehicle: Buick Lesabre)

3.4 Summary

This chapter presented the design of LTV controllers for the degraded mode vehicle lateral control under fault in front or rear magnetometers. The vehicle lateral dynamics from the steering input to either front or rear magnetometer output is sensitive to the longitudinal velocity; thus, time varying controllers are required in order to meet the performance cirteria. A novel method for LTV controller design, feedback linearization with mismatched observers, is proposed to especially target at the control of LTV systems with weakly damped zeroes or RHP zeros. Feedback linearization provides a simple yet effecive way of gain scheduling, and the mismatch observer prevents the weakly damped zeros or the RHP zero of the vehicle lateral dynamics from being contained in the internal dynamics. The application of the method in the design of the degraded mode vehicle lateral control was detailed in this section and both the FMB controller and the RMB controller have been designed. The stability of the

overall closed-loop system is examined based on the concept of quadratic stability. For the FMB control, a single mismatched observer designed at $20m/s$ is capable of achieving quadratic stability over the whole operating range; for the RMB control, however, one mismatched observer can not achieve stability over the whole operating range. Hence, several mismatched observers have been designed and gain scheduling is employed. Experiments have been conducted at Richmond Field Station, and the results demonstrate the effectiveness of the controller design.

4 Transition Behavior between the Normal and Degraded-Mode Controllers

In fault management systems, based on fault detection and isolation (FDI) and system reconfiguration, the control system is switched to the corresponding degraded mode control once a fault has been detected. Prerequisites for a successful fault management system include a reliable FDI module, degraded mode control systems that guarantee stability and performance under fault, and benign transition behavior between the normal control system and the degraded mode control system. In this report, the specific fault considered is the magnetometer failures, and it has been assumed that a reliable FDI module has been developed to detect magnetometer failures. The research presented in previous sections focuses on the design of the degraded mode controllers under fault in either front or rear magnetometers. Whenever front or rear magnetometer failure is detected, lateral control will be transfered from the nominal controller to the corresponding degraded mode controller. Now that it has been demonstrated that the degraded mode controllers are capable of achieving satisfactory performance under magnetometer failures, it has to be ensured that no abnormal transition behavior takes place as the degraded mode controllers take control of the faulty system.

It should be clarified that the transition behavior starts from the moment a fault

occurs, not the moment the degraded mode controller actually takes control of the faulty system. The time difference between the occurance of a fault and the controller switch is determined by how fast the FDI module can detect the fault and how long it takes the fault management system to make the decision of controller switch. During this period, the faulty system will still be under the control of the normal mode controller. As demonstrated in previous research, when rear magnetometers fail, the performance of the normal mode controller deteriorates; moreover, when front magnetometers fail, the normal mode controller can not guarantee stability. If the delay in both the fault detection and the decision making of the fault management system is too long, the faulty system may go out of control before the degraded mode controller acts. For example, the vehicle lateral error gets so large that the error is out of the sensing range of the remaining functional magnetometers. Hence, it is critical to research on how much delay is allowed for the faulty system to be still tamable by the degraded mode controller.

A second issue in transition behavior is the actual happening of the controller switch. Generally, the degrade mode controller and the normal mode controller will provide different control forces, and a direct switch may result in a sudden brupt change in the control input and impair riding comfort. Some kind of switching methods might be employed to smooth the transition. Another question concerns with how fast the degraded mode controller can bring the faulty system to the steady and optimal performance that it could achieve in the faulty situation. This, of course, depends on how good the degraded mode controller itself is. With a given degraded mode controller, the answer to this question depends on the system initial conditions. Intuitively, it would be most effective to have the degraded mode controller already working at its steady state when the switch takes place, i.e., the degraded mode controller can be runned along with the normal mode controller no matter faults occur or not. However, this ineveitably adds load on the control computation. From the perspective of the overall fault management system, it would be rather impractical

to keep all degraded mode controllers running all the time. Another possiblity is to retain the same states of the controllers while switching. To do that, the degraded mode controller must have the same structure with the normal mode controller. This would be a rather strict constraint on the degraded mode controller design. In our specific case, due to the sensor failure, the look-ahead scheme, which is the basis of the normal mode controller, is no longer applicable for the degraded mode controller. In fact, the structure of the degraded mode controllers designed can not be associated with that of the normal mode controller. A more flexible and effective way is to choose the initial value of the degraded mode control based on Initial Value Compensation (IVC) techniques.

In summary, the research on the transition behavior has two objectives:

- To design switching methods to achieve satisfactory transition behaviors, and to investigate IVC techniques for better transient behaviors if necessary.
- To investigate the effect of delay in fault detection on the transition behavior and to provide quantitative information on the amount of allowable delay without much sacrifice on performance.

In this section, techniques for controller switching and IVC are reviewed, and simulations and experiments are conducted to evaluate the transition behavior, and the effects of the delay are examined.

4.1 Switching Techniques and Initial Value Compensation

4.2 Switching Techniques

The simplest way of controller switch is a direct switch in the control input. The main disadvantage of this direct switch would be the sudden change in the input and bumpy transition behavior of the system. To smooth the transition, linear interpolation can be introduced. In the case of switching from the normal mode control to the degraded

mode control, the linear interpolation can be:

$$u_{in} = \alpha(t)u_{normal} + (1 - \alpha(t))u_{degraded} \tag{42}$$

where u_{in} is the actual control input to the plant, u_{normal} and $u_{degraded}$ are the control forces calculated by the normal mode controller and the degraded mode controller, respectively. As $\alpha(t)$ changes from 1 to 0 during $[t_0, (t_0 + t_s)]$(t_0 stands for the time the switching starts and t_s is the switching duration time), the control is graduately switched to the degraded mode controller.

The switch duration time t_s determines how fast the control is switched and the profile of $\alpha(t)$ affects how smooth the actual input would be during the transition. A longer switch duration t_s generally provides more gradual change in the input, but then the combined control of the normal controller and the degraded mode controller may not be effective enough to prevent the faulty system from exhibiting abnormal behavior. Additionally, fast switch will be more effective to ensure safety and adequate performance of the faulty system, but the temperary switching behavior could be rugged. The determination of both t_s and $\alpha(t)$ is conducted to obtain an optimal tradeoff between these two conflict goals. However, generalized theoretical optimization approaches are rare due to the complexity of the problem. Currently, most effective and cost-wise way may be trial and error for specific individual applications.

4.2.1 Initial Value Compensation

Initial Value Compensation (IVC) was first proposed for the Mode-Switching Control (MSC) in hard disk control by Yamaguchi, et al. [15], [16]. The MSC involves a control system that includes several controllers with different structures and a switching function that switches the control from one controller to another according to certain conditions. One of the design issues for the MSC is the method of switching between controllers and IVC is a mechanism used to improve transient characteristics after mode-switching. Under IVC, the switching problem can be treated as a controller de-

sign with non-zero initial conditions (though the initial values may also be introduced as an additional input added at switching).

The state equations of the controller and the plant in a tracking problem are given by:

$$\begin{aligned} X_p(k+1) &= A_p X_p(k) + B_p u(k) \\ y(k) &= C_p X_p(k) \end{aligned} \tag{43}$$

$$\begin{aligned} X_c(k+1) &= A_c X_c(k) + B_c(r(k) - y(k)) \\ u(k) &= C_c X_c(k) + D_c(r(k) - y(k)) \end{aligned} \tag{44}$$

where X_p is an mth-order state vector of the plant, X_c is an nth-order state vector of the controller, u is a control input to the plant, r is a reference, y is a controlled variable, and A_p, B_p, C_p, A_c, B_c, C_c, and D_c are $m \times m$, $m \times 1$, $1 \times m$, $n \times n$, $n \times 1$, $1 \times n$, and 1×1 real matrices respectively. $k = 0$ indicates the time at mode switching.

The z-transform solution to Eqs. 43 and 44 with non-zero initial conditions is as follows:

$$y(z) = \frac{N_r(z)}{D(z)} r(z) + \frac{N_p(z)}{D(z)} X_p(0) + \frac{N_c(z)}{D(z)} X_c(0) \tag{45}$$

where

$$D(z) = det[zI - A], \quad A = \begin{bmatrix} A_p - B_p D_c C_p & B_p C_c \\ -B_c C_p & A_c \end{bmatrix} \tag{46}$$

and $N_p(z)$ and $N_c(z)$ are $1 \times m$ and $1 \times n$ polynomial matrices respectively, represented as:

$$\begin{bmatrix} N_p(z) & N_c(z) \end{bmatrix} = \begin{bmatrix} C_p & 0 \end{bmatrix} adj(zI - A)z \tag{47}$$

where $D(z)$ and $N_r(z)$ are scalar z polynomials and $N_p(z)$ and $N_c(z)$ are $1 \times m$, $1 \times n$ polynomial matrices respectively.

One method to set the initial values of the controller state variables is to minimize a cost function which is an integral of the squares of state variables such as velocity and position, eg. $J = \sum_{k=0}^{\infty} X(k)^T Q X(k)$, where $X(k) = \begin{bmatrix} X_p(k)^T & X_c(k)^T \end{bmatrix}^T$ and Q

is a weighting coefficient matrix. The cost function can be transformed to a square of the inital values $J = X(0)^T P X(0)$ by a discrete Lyapunov Equation where $P = \begin{bmatrix} P_{11} & P_{12} \\ P_{21} & P_{22} \end{bmatrix}$ is defined by $A^T P A - P = -Q$ and is a positive definite matrix. By differentiating J by $X_c(0)$, the optimal initial state variables can be solved as $X_c(0) = -P_{22}^{-1} P_{12}^T X_p(0)$. At mode-switching, the state variables of the controller is set to $X_c(0)$.

The second method is to directly relate the initial state variables of the controller with those of the plant by introducing an $n \times m$ real coefficient matrix K: $X_c(0) = KX_p(0)$, such that Equation 45 becomes:

$$y(z) = \frac{N_p(z) + N_c(z)K}{D(z)} X_p(0) \tag{48}$$

where r has been set to 0 for simplicity[17]. Eq. 48 shows that the z-transform of the output sequence $y(k)$ with respect to the non-zero initial conditions can be shifted to the desired value by selecting an appropriate K to cancel undesired poles. Suppose that the closed-loop poles λ_k ($k = 1, \ldots, j$; where $1 \leq j \leq$(order of the controller)) cause slow transient responses and are to be cancelled. Substitute $z = \lambda_k$ into the polynomial of the numerator of Equation 48 for each element of $X_p(0)$ and set it to zero; then we will have j equations for the unknown $K(n, k)(k = 1, \ldots, j)$ matrix. $K(n, k)$ can then be solved under the condition of either $j = n$ or the resetting of the residual state variables of the controller when $n > j$ [17].

The third method is to add an additional input at mode-switching so that the desirable poles of the transient response can be provided. Here, the additional input r' is added after the controller output and can be represented as $r'(z) = \frac{n(z)}{d(z)} X_p(0)$, where $n(z)$ is a polynomial, and $d(z)$ is a stable polynomial. And $X_c(0) = 0$. The transfer function between $r'(z)$ and $y(z)$ is assumed to be $N_r(z)/D(z)$ ($N_r(z)$ and $D(z)$ are polynomials); then Equation 45 is represented as:

$$y(z) = \frac{N_r(z)n(z) + N_p(z)d(z)}{D(z)d(z)} X_p(0) \tag{49}$$

Since the roots of $D(z)$ do not always have desirable roots for the transient response, it is desired that all roots of $D(z)$ be cancelled by zeros and that $d(z)$ should have desirable (stable, of course) poles. Hence,

$$d(z) = d'(z)d_m(z), \text{ with } d_m(z) = (z-\eta_1)(z-\eta_2)\dots(z-\eta_l) \tag{50}$$

$$\Longrightarrow y(z) = \frac{N_r(z)n(z) + N_p(z)d'(z)d_m(z)}{D(z)d'(z)}\frac{1}{d_m(z)}X_p(0) \tag{51}$$

Divide $N_r(z)$ into $N'_r(z)N^u_r(z)$ where the roots of $N^u_r(z)$ are unstable zeros and the roots of $N'_r(z)$ are stable ones. Choose $d'(z) = N'_r(z)$, we will have:

$$y(z) = \frac{N^u_r(z)n(z) + N_p(z)d_m(z)}{D(z)}\frac{1}{d_m(z)}X_p(0) \tag{52}$$

Let $n(z)$ be a polynomial with order $m+n-1$: $n(z) = a_{m+n-1}z^{m+n-1} + a_{m+n-2}z^{m+n-2} + \cdots + a_1 z + a_0$, and solve the following equations for $n(z)$.

$$N^u_r(\lambda_i)n(\lambda_i) + N_p(\lambda_i)d_m(\lambda_i) = 0, \quad (i = 1, \dots, m+n) \tag{53}$$

Thus, the roots of $N^u_r(z)n(z) + N_p(z)d_m(z)$ include all the roots of $D(z)$ that are λ_i $(i = 1, \dots, m+n)$ and the transient response is dominated by the desirable poles.

The first two IVC designs are very easy to implement and various applications have demonstrated good performance. However, it should be noted that the disturbance-rejection ability is reduced by the pole assignment and the steady-state characteristics is not considered in the design. The third method also provides good performance, but its implementation is more complicated.

4.3 Simulation and Experiments on Transition Behavior

The purpose of switching techniques and Initial Value Compensation is to achieve smooth transition behavior. First, the transition behavior under the simplest controller switch method, direct input switch to the degraded mode controller with zero initial conditions, is examined. Simulations are conducted with the Front-Magnetometer-based (FMB) controller and the CG (mass center) based controller.

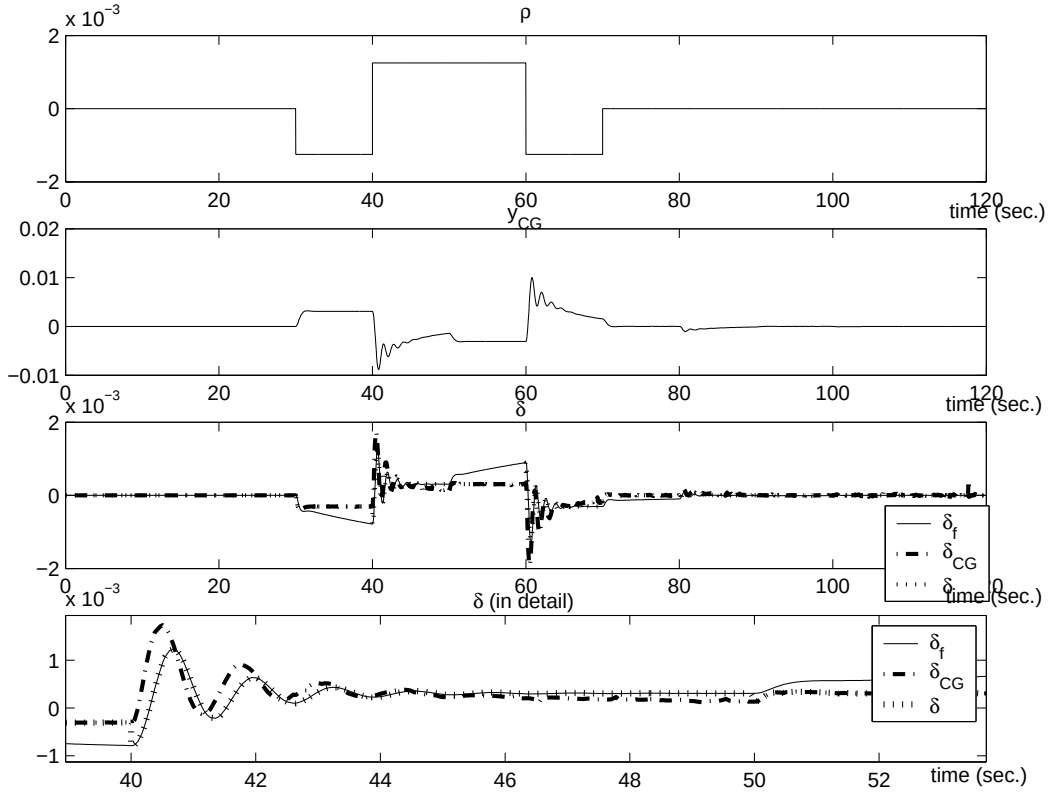

Figure 23: Simulation result of switch between front controller and cg controller every 10 sec)

Every 10 seconds, the control input to the plant is switched between the FMB controller and the CG controller (Figure 23). Simulation shows that the difference between the control force from the FMB controller and the CG controller is small.

Experiments on the transition behavior were conducted at the Clow's Landing with the same Buick LeSabre car with which experiments on the FMB controller and the RMB controller were conducted. Again, the controller switch was between the FMB controller and the CG controller, and the switch took place every 200 markers (i.e., approximately every 6 seconds). Figure 24 and Figure 25 are the results assuming that there is no delay in FDI and fault management decision making. The two figures are from the same experimental run. From Figure 25, it is impossible to tell when the switch happened from either the lateral error signal (y_f and y_r) or the steering input

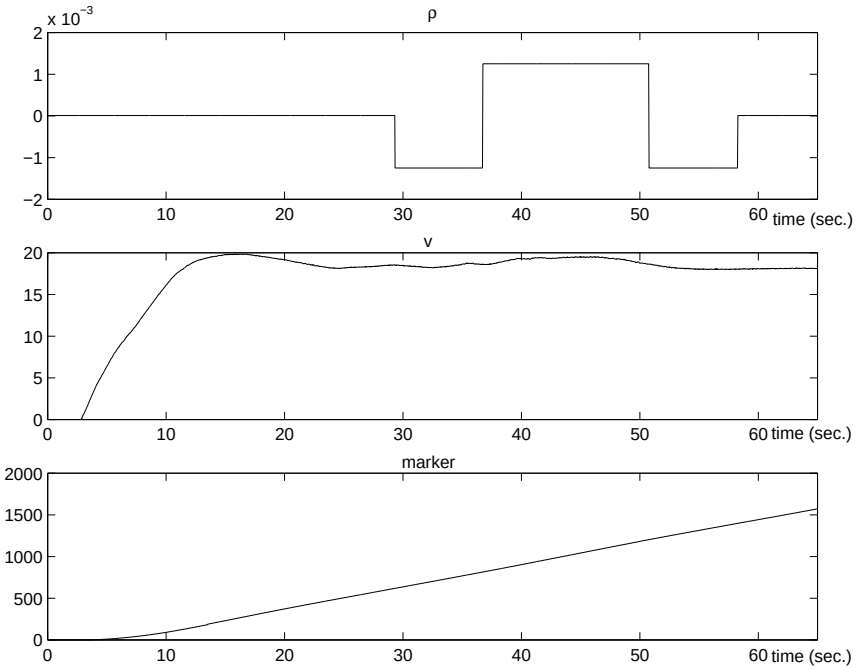

Figure 24: Experiment result a (switch between front controller and cg controller every 200 markers,without delay)

(δ). The transition was not noticeable by the author and the driver from PATH who were sitting in the car.

Experiments on the transition behavior without delay suggests that the transition is rather smooth and more complicated switching techniques or Initial Value Compensation are not necessary in this particular case. The next question to be answer is how much delay can be tolerated without sacrifising smoothness and safety.

Experiments on the transition behavior with delay were then conducted with the FMB controller and the CG controller. Every 200 markers (approximately every 6 seconds), controller switch took place. For the switch from the CG controller to the FMB controller, it is assumed that a delay took place and the CG controller would continue the control with only the measurements of front magnetometers during the delay period. Figure 26 and Figure 27 shows the result with delay of 10 markers. Again, it is almost impossible to detect the switch from the lateral errors and the

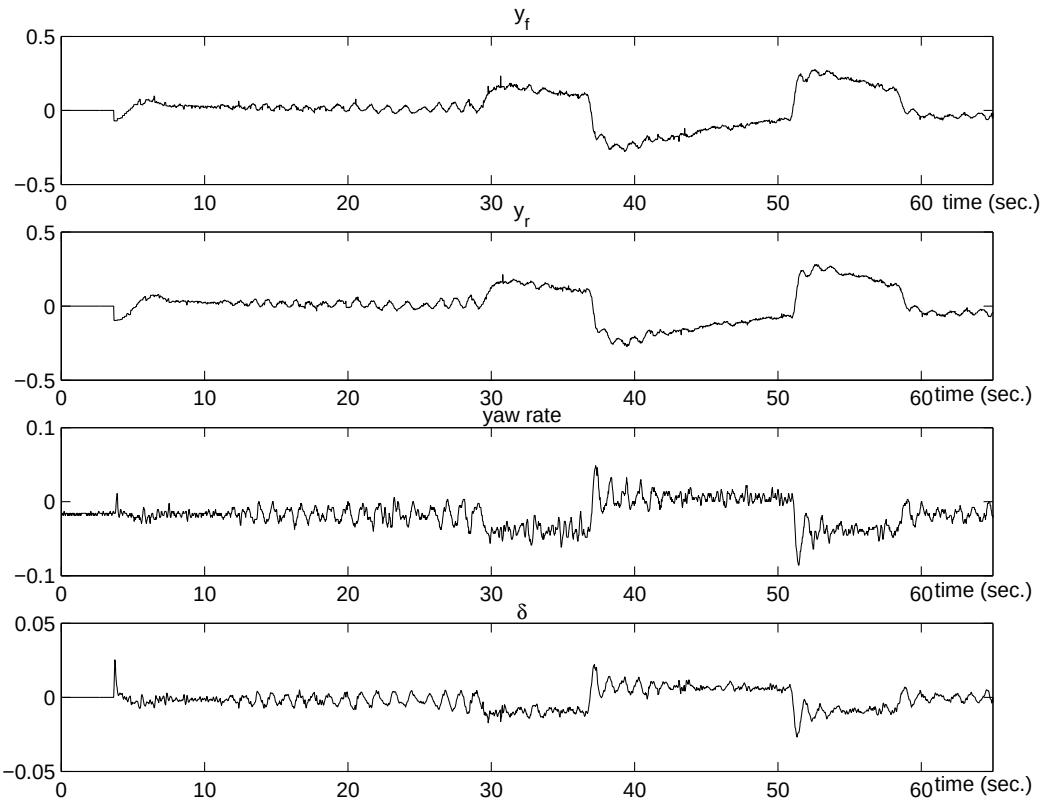

Figure 25: Experiment result b (switch between front controller and cg controller every 200 markers,without delay)

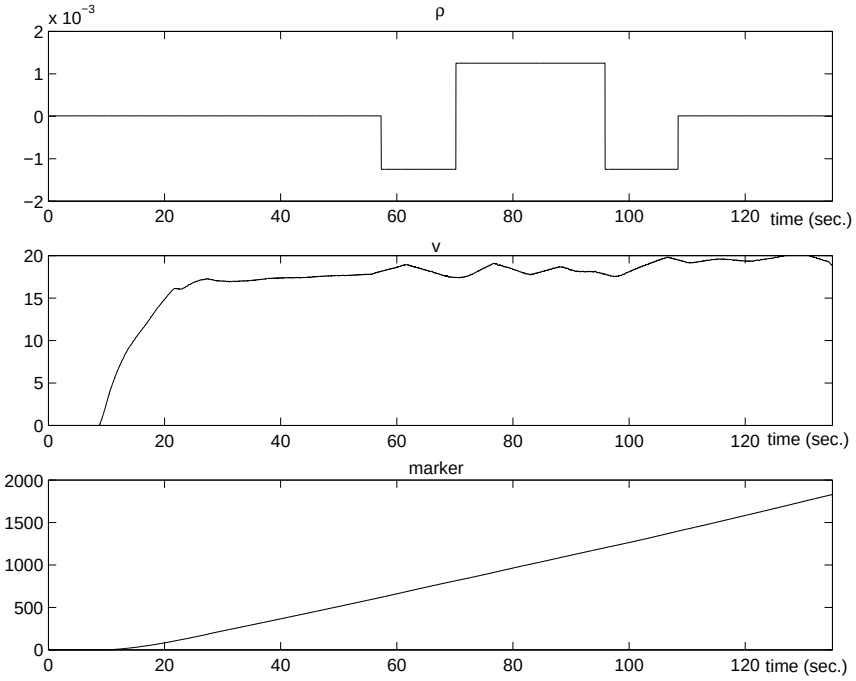

Figure 26: Experiment result a (switch between front controller and cg controller every 200 markers,with delay)

control input, that is, the switching behavior is smooth enough with delay at least up to 10 markers, which corresponding to delay of approximately 0.3 second.

4.4 Summary

Smooth transition behavior, along with a reliable FDI module and robust normal mode control and degraded mode control, is crucial for a successful fault tolerant control system. The transition behavior starts at the moment a fault occurs and ends when the degraded mode control system reaches its steady state. The transition behavior is affected by the delay in the FDI module, the robustness of the normal mode controller to accomodate the fault during the delay period, and the capability of the degraded mode controller to bring the faulty system to satisfactory performance from relative large deviation due to the fault and the delay. To smooth the transition

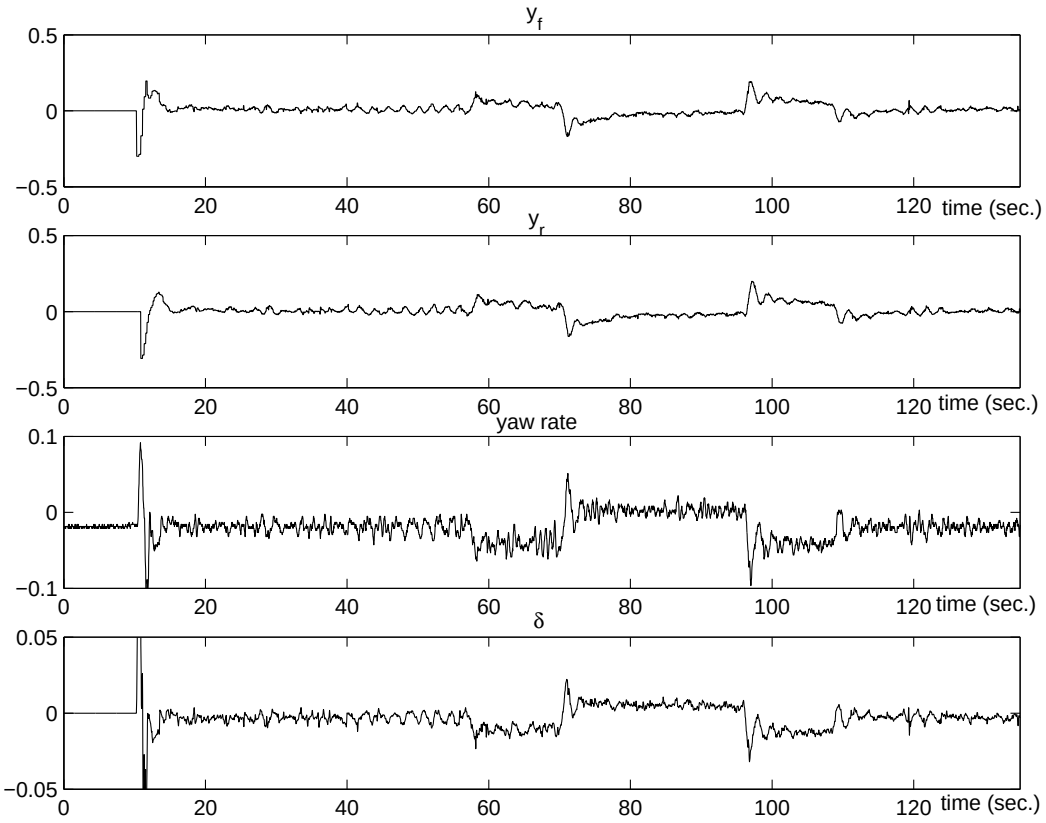

Figure 27: Experiment result b (switch between front controller and cg controller every 200 markers,with delay)

behavior, some kind of switching mechanism and choice of initial value for the states of the degraded mode controller can be employed.

In this section, switching mechanisms such as linear interpolation and Initial Value Compensation (IVC) have been reviewed. Linear interpolation provides a simple combination of the control forces from the normal mode controller and the degraded mode controller while IVC techniques provide more systematic ways to achieve desirable transition behavior by determining the initial value of the states of the degraded mode controller. Yet, for the specific application described in this report, the robustness of both the normal mode controller and the degraded mode controller is adequate to provide smooth transition behavior even with the simplest direct switch of the control force. It then makes the use of more complicated switching mechanisms practically unnessesary.

Simulations and experiments have been conducted to investigate the transition behavior between the Front-Magnetometer-Based controller designed in Section 3 and a CG based controller. Direct switch of the control force is employed and no IVC is involved. Both simulation and experimental results have shown that the transition behavor is very smooth with up to at least 10 markers detection delay.

5 LIDAR Based Autonomous Vehicle Following

5.1 Introduction

Compared to road following control, vehicle following control schemes have received much less attention in past research. This makes autonomous vehicle following a relatively new approach for vehicle steering control. Autonomous vehicle following achieves vehicle lane-keeping performance by controlling the vehicle to follow the preceding vehicle, assuming that the preceding vehicle is on the desired track with no lateral error nor relative yaw error with respect to the road centerline. In this control scheme, the lateral controller sets the steering command according to the vehicle's

relative position with respect to the preceding vehicle. Hence, no road infrastructure is required for the implementation of the control scheme. Autonomous vehicle following may serve as a back-up system for the road following based vehicle lateral control schemes in the case of sensor failures, and it may also work as an independent drive-assist system. In order to control the vehicle to follow the preceding vehicle, autonomous following schemes require the measurements of the relative distance between the two vehicles. This is achieved by the on-board laser scanning radar sensor (LIDAR) in this project.

Algorithms have been developed in past for autonomous vehicle following. Fujioka and Omae described five vehicle following control algorithms by using a laser scanning radar[4], and Gehrig and Stein developed a trajectory-based algorithm for car following[5]. These algorithms have to depend on a combination of many on-board sensors such as yaw rate sensor, accelerator, and sensors that detect the vehicle's relative position with respect to its preceding vehicle. Since no road reference system was available in their research, the lane-keeping performance for autonomous vehicle following has not been studied.

In practice, the preceding vehicle is not necessarily on the desired track. The lateral error and yaw of the preceding vehicle will be passed on to the following vehicle, when the following vehicle follows the path of the preceding vehicle. Since it is impossible for the controlled vehicle to follow the preceding vehicle perfectly, the controlled vehicle will have larger lateral errors than the preceding vehicle. If there are many vehicles under autonomous vehicle following control in a platoon, and each of them follows its preceding vehicle except the leading one, the lateral errors of the following vehicles may be accumulated. Thus the string stability problem of the platoon must be studied in the lateral direction.

This section first briefly introduces the LIDAR sensor and its processing algorithm, then it describes the design of controllers for LIDAR-based autonomous vehicle following, including a lead-lag controller and a H_∞ controller. By analyzing the

experimental results for the two control laws, with different control algorithms for the leading vehicle, the section tries to reveal the error propagation problem in practice. The error propagation/string stability problem is further studied by simulations and analysis. An inter-vehicle communication based solution is proposed, and the lane-keeping performance of the system is evaluated by real-time experiments involving two vehicles. Finally, simulations are conducted to verify the system performance for a platoon of four vehicles.

5.2 LIDAR and Data Processing

For autonomous vehicle following, a laser scanning radar sensor (LIDAR) has been used to measure the relative distance from the leading vehicle to the following vehicle. The LIDAR sensor consists of a laser diode, a scanning mechanism, and a receiver. The laser diode emits laser beams to the roadway. The scanning mechanism is a rotating prism, and it makes the laser beams scan in the horizontal plane. If the laser beams hit any reflective object on the roadway, they will bounce back. The reflected laser beams can be detected by the built-in receiver. The distance from the sensor to the object is measured according to the amount of travel time and velocity of the light. Since the laser beams scan in the horizontal plane with constant steps, the orientation of the object can also be measured by counting the number of the scanning steps. Hence, the position of an object is uniquely defined in two dimensional space. The measured position is written in polar coordinates. In autonomous vehicle following, a target with a reflective surface is fixed on the rear bumper of the leading vehicle, and a LIDAR sensor is installed on the following vehicle; therefore, the relative distance between the two test vehicles can be measured.

When the laser beam scans, it detects anything reflective on the roadway. Since there are numerous reflective objects and surfaces in the environment, the LIDAR sensor returns one set of measurements in every scanning step. For each sampling period, the LIDAR sensor returns 80 sets of measurements, most of which are not

related to the desired target. Extraction of the useful information about the real position of the desired target from the sensor measurements is a key research issue in autonomous vehicle following.

At the first thought, picking one measurement that has the strongest intensity value seems to be a natural idea. However, two main concerns arise about this method. First, the intensity data is quite rough, because it is an integer varying from 0 to 31. Hence it is not practical to rely on the intensity data to make the decision. Second, picking only one measurement is of high risk, because the algorithm is very likely to keep tracking a wrong target if a wrong selection is made at some sampling point in the past.

To determine the actual position of the target of interest, a probability data association method proposed by Bar-Shalom[2] has been applied to process the LIDAR measurements. The fundamental idea of the data processing algorithm is to combine all the validated measured data according to their probabilities of being the correct measurement to update a Kalman filter. The data points that are more likely to be the correct measurements receive higher weights in the algorithm than other data points. This is based on the assumption that all measurements are normally distributed around a predicted point. Details of this algorithm have been described in the previous annual report.

As shown in Fig.28, L and y_{L_i} denote the longitudinal and lateral distance, between the $(i-1)$th and ith vehicles, measured by the sensor. y_{Ri-1} represents the absolute deviation of the $(i-1)$th vehicle at the position where the target is placed. Let y_{Vi} denote the virtual absolute deviation of the ith vehicle at the distance L ahead of the vehicle CG. Then,

$$y_{Vi} = C_2 \xi_i \tag{54}$$

and

$$y_{Ri-1} = C_1 \xi_{i-1} \tag{55}$$

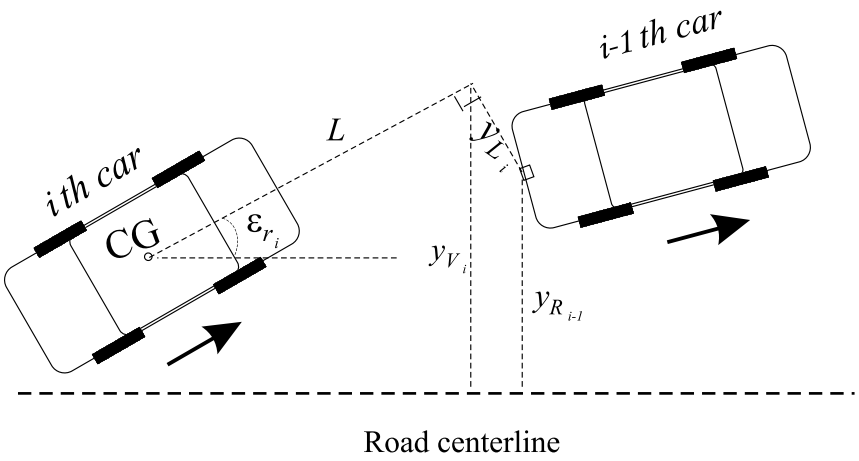

Figure 28: Autonomous vehicle following measurement scheme

where ξ_i denotes the state vector of the ith vehicle, and

$$C_2 = (\ 1 \quad 0 \quad L \quad 0\ ) \tag{56}$$

$$C_1 = (\ 1 \quad 0 \quad -h_2 \quad 0\ ) \tag{57}$$

The lateral measurement by the autonomous vehicle following sensor of the ith vehicle can be represented as

$$y_{Li} = \frac{(y_{Vi} - y_{Ri-1})}{cos\ \epsilon_{ri}} \tag{58}$$

where ϵ_{ri} is the yaw angle of the ith vehicle relative to the road centerline. It is further assumed that ϵ_{ri} is small. Then,

$$y_{Li} \approx (y_{Vi} - y_{Ri-1}) \tag{59}$$

The above equations show that the measurement by the autonomous vehicle following sensor is essentially a look-ahead measurement, i.e. the sensor measures the lateral deviation at a point with distance L ahead of the vehicle's CG. Thus, using the sensor measurement as the feedback signal to the controller automatically provides similar benefits as that produced by the virtual look-ahead scheme in [6][7].

It is also clear from the above equations that the platoon that consists of the lead and the following vehicles becomes an interconnected system. For this interconnected

system, stability of each system component, i.e. each vehicle, cannot guarantee the stability of the entire system because the system components are not independent. Instead, string stability needs to be considered.

5.3 Setup for Experimental Study

A platoon of two Buick vehicles were used in the experimental testing on a test track at the Richmond Field Station, University of California, Berkeley. The maximum allowable speed on the test track was 25MPH. The track consisted of many curves, but no preview of the road curvature was used in the testing. The unique feature of this track was that there were equally-spaced magnetic markers buried under the road centerline. Both test vehicles were equipped with two sets of magnetometers, one under the front bumper and the other under the rear bumper. Hence the magnetometer measurements represent the vehicles' lateral deviation from the road centerline. The two vehicles were manually driven in the longitudinal direction, and the space between them was controlled manually by the driver who operated the following vehicle. In the testing, the leading vehicle was automatically steered based on the magnetometer measurements to follow the magnetic markers, i.e. the road centerline, and the following vehicle used the autonomous vehicle following based steering control. The magnetometer measurements on the following vehicle were never used to set the steering control input, but they were collected to evaluate the vehicle's tracking performance in the road-fixed coordinate frame. Comparison between the magnetometer measurements of the two vehicles will further reveal the potential error propagation problem in autonomous vehicle following.

5.4 Lead-Lag Control

The controller design starts with the assumption that there is no communication between the leading and the following vehicles. Thus the dynamics of the leading vehicle are treated as unknown disturbances to the following vehicle. The input to

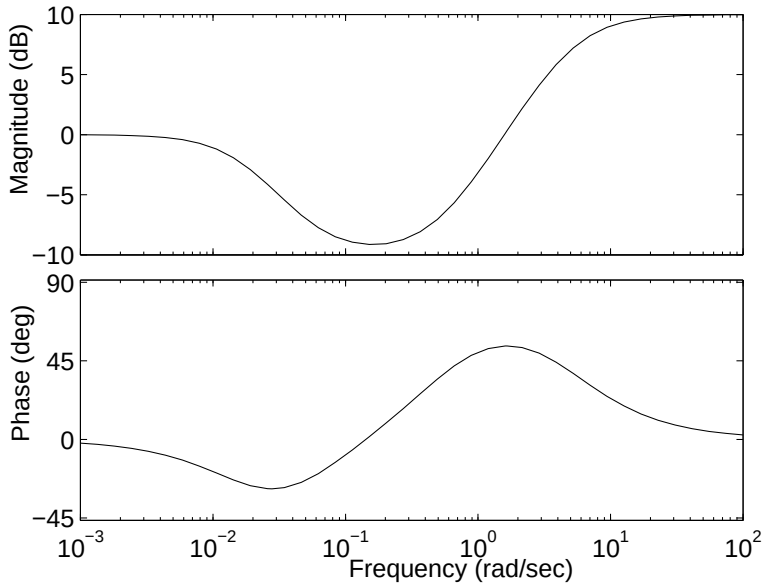

Figure 29: Bode plot of the autonomous vehicle following controller

the controller is the relative lateral distance measured by the LIDAR sensor, and the design of the autonomous vehicle following controller is similar to that for a road following controller, except that the vehicle dynamic system has a large and fixed look-ahead distance. The first control algorithm used here is a lead-lag controller. The control law is:

$$\frac{(2s+1)(18s+1)}{(0.2s+1)(56.98s+1)} \tag{60}$$

The Bode plot of this controller is shown in Fig.29.

Figures 30 and 31 show the experimental results of the controlled vehicle. The vehicle following performance is evaluated by the measurements from both the LIDAR and the magnetometer sensors. It can be seen from the results that the controlled vehicle is still kept in the lane by following the lead vehicle. However, there is a negative bias associated with the lateral position of the following vehicle, relative to the road centerline. The control law of the leading vehicle was one of the existing steering controllers. Due to technical difficulties, the sensor measurements of the two vehicles when the leading vehicle was using this control law could not be synchronized.

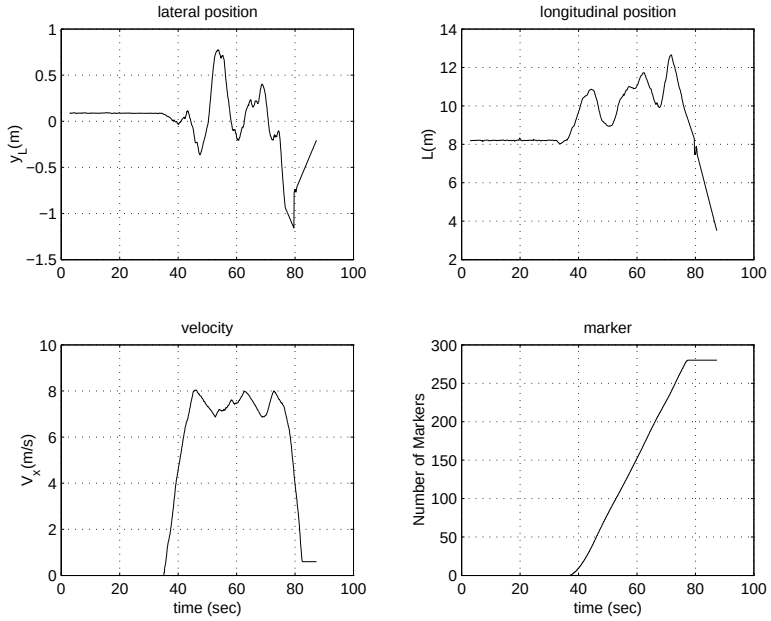

Figure 30: Lead-lag control experimental results of following vehicle when the tracking error of the leading vehicle has a negative bias: lateral and longitudinal distance measured by LIDAR sensor, vehicle velocity, and recording of magnetic markers

Hence the experimental results of the leading vehicle are shown separately in Fig.32. Note that there is also a small negative bias in the lateral deviation of the leading vehicle. By comparing the lane-keeping performance of the two vehicles, one may conclude immediately that the performance of the following vehicle is worse than that of the leading one; further, one may guess that the large bias for the following vehicle may be caused by the small bias of the leading vehicle. Intuitively, this is a reasonable hypothesis because any lateral error of the leading vehicle may be transmitted to the vehicle that follows its trajectory. In general, the tracking error should become worse in the following vehicle.

5.5 H_∞ Synthesis

The second controller is designed by using H_∞ synthesis. In this design, the control algorithm is required to calculate the correct steering angle at the tires in order to

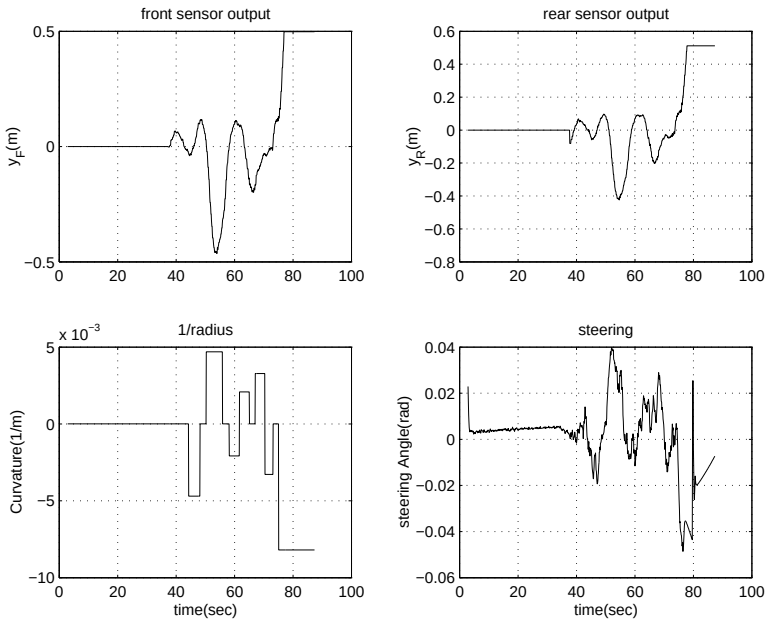

Figure 31: Lead-lag control experimental results of following vehicle when the tracking error of the leading vehicle has a negative bias: measurements from front and rear magnetometers, road curvature, and steering angle

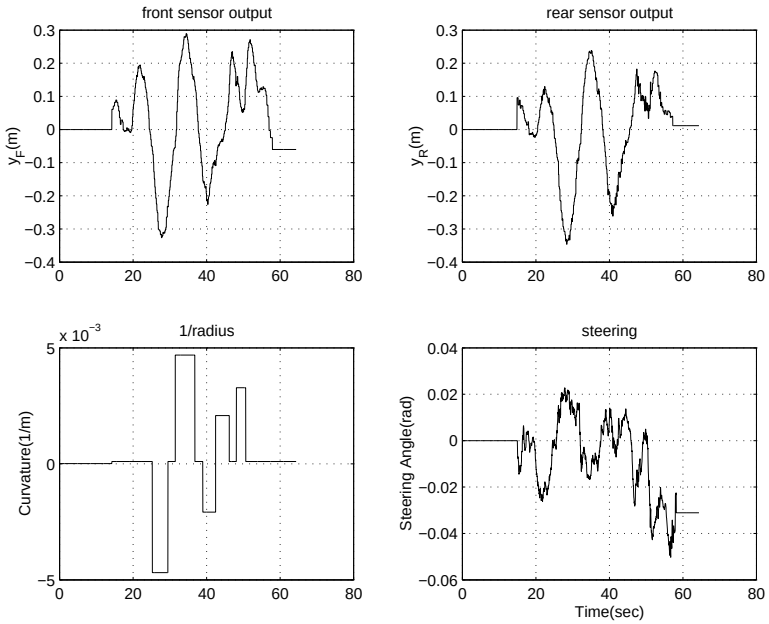

Figure 32: Experimental results of lead vehicle associated with a negative bias: measurements from front and rear magnetometers, road curvature, and steering angle

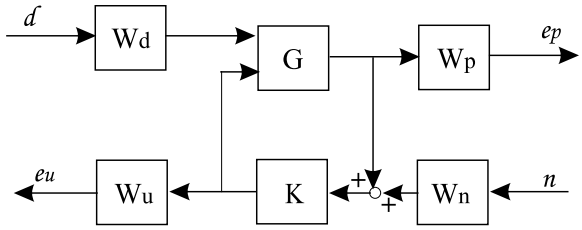

Figure 33: H_∞ synthesis structure

regulate the lateral deviation, in the presence of the unknown road curvature and sensor noise. The steering input should be kept small considering the saturation problems and passenger discomfort. As shown in Fig.33, G is used to represent the vehicle lateral dynamics described in Section 1, the road curvature is treated as an unknown disturbance d, n denotes the sensor noise, and the weighting functions W_p, W_n, W_u, and W_d are used to place suitable weights at various frequency ranges. e_p and e_u are the weighted vehicle lateral deviation and steering input, respectively. The goal of this design is to minimize the effects of the external disturbances d and n on the weighted system outputs in terms of the H_∞ norm.

The weighting functions are chosen according to standard considerations in H_∞ synthesis design. Penalty on the lateral error should be high at low frequencies for good tracking performance, and low at high frequencies to avoid exciting the unmodeled high-frequency dynamics. For the same reason, penalty on the steering input should be high at high frequencies. W_n and W_d are set constant to avoid producing a high-order controller, and they are chosen according to the system performance requirements. The weighting functions chosen for this design are as follows.

$$W_d = \frac{7}{200} \tag{61}$$

$$W_n = \frac{1}{50} \tag{62}$$

$$W_p = 0.1\frac{s+1}{s+0.003} \tag{63}$$

$$W_u = 2000\frac{s+10}{s+120} \tag{64}$$

The controller thus designed is of sixth-order.

The control algorithm for the leading vehicle was redesigned in a lead-lag form, and this also enabled the synchronization of the recording of the two vehicles' performance. Figures 34 and 35 show the experimental results of the autonomous vehicle following control while the redesigned controller for the lead vehicle and the H_∞ controller for the following vehicle were used. Both vehicles traveled up to 20MPH during the testing. Note that the steering controller of the leading vehicle was different from that in the previous testing. The maximum tracking error of the lead vehicle was about $10cm$ from the road centerline, and the maximum tracking error of the following vehicle was about $25cm$ from the road centerline. Therefore the tracking performance of this controller is significantly better than the previous one. From the results, it is clear that the lateral deviation of the following vehicle now has a large positive bias. It is also computed that the average of the lateral deviation of the lead vehicle was about positive $5cm$, and this could be the reason for the positive bias in the tracking error of the following vehicle. Again the results have verified the previous hypothesis that the lateral error of the lead vehicle indeed has been transmitted to the following vehicle. It is clear that without additional information, autonomous following algorithm can not adjust the bias in real time.

5.6 String Stability in Autonomous Following

The above experimental results have shown that tracking errors of the leading vehicle may be passed on to the following vehicle and result in larger errors of the following vehicle. One may still wonder whether this is true for a larger platoon of vehicles. This problem is illustrated by simulation results for a platoon of four vehicles. In the simulation, the first vehicle of the platoon used a road-following control algorithm, and the other vehicles were under autonomous vehicle following control, each one following its preceding vehicle. The simulated road consisted of two curves, each with curvature of $\pm\frac{1}{800m}$ respectively, as shown in Fig.36. The simulated vehicle speed was $30m/sec$

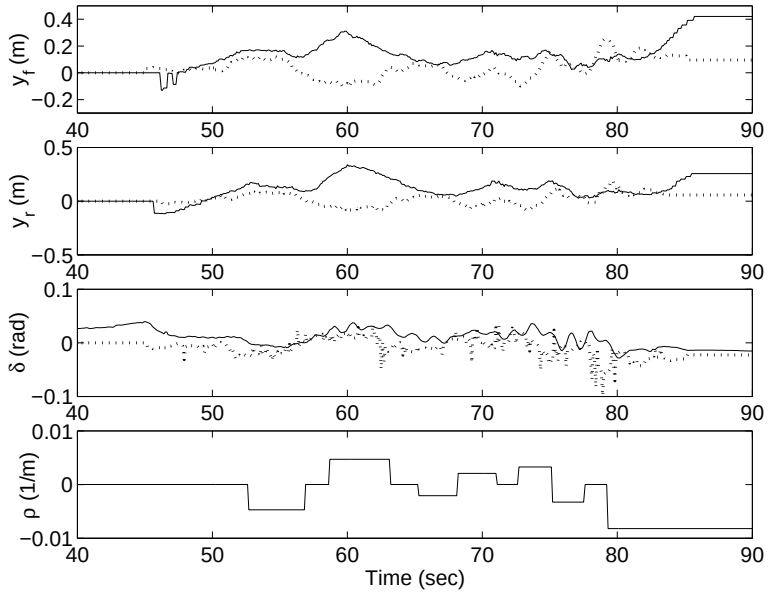

Figure 34: H_∞ control experimental results for autonomous vehicle following when the tracking error of the leading vehicle has a positive bias: front, rear magnetometer outputs, steering angle, and road curvature. (solid: following vehicle; dashed: lead vehicle)

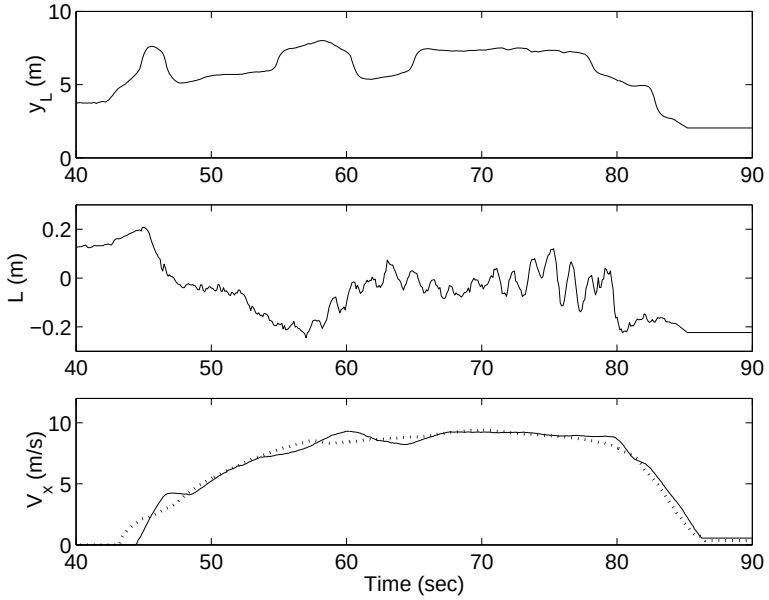

Figure 35: H_∞ control experimental results for autonomous vehicle following when the tracking error of the leading vehicle has a positive bias: lateral, longitudinal distance between the two test vehicles measured by LIDAR, and vehicle speed (solid: following vehicle; dashed: lead vehicle)

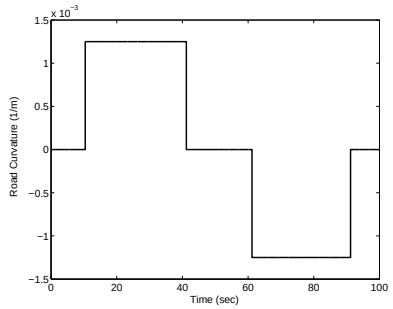

Figure 36: Simulated road curvature)

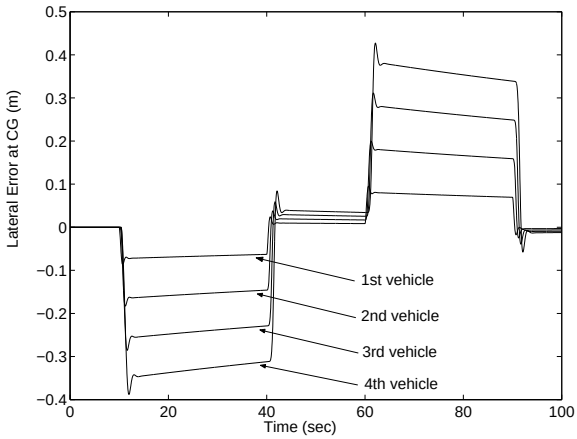

Figure 37: Simulation results for autonomous vehicle following control without inter-vehicle communication (for a platoon of four vehicles)

for all vehicles. The space between adjacent vehicles was $10m$. The simulation results are shown in Fig.37. It can be seen that the lateral deviation accumulates in the upstream direction of the platoon, i.e. the lateral error of each following vehicle is larger than that of its preceding vehicle. The accumulation of tracking errors is caused by the superposition of the tracking errors of the leading vehicle and the errors in autonomous vehicle following. As the number of the following vehicles increases, the tracking errors of the vehicle at the end of the platoon increase. Note that the control system of each vehicle in the simulation is stable, but the simulation results still indicate the stability issue for vehicle platoons, i.e. string stability.

In order to analyze the string stability problem in autonomous vehicle following,

the following definitions and theorem from Swaroop and Hedrick [12] are introduced.

Consider the following interconnected system:

$$\dot{x}_i = f(x_i, x_{i-1}, \cdots, x_{i-r+1}) \tag{65}$$

where $i \in N$, $x_{i-j} \equiv 0$, $\forall i \leq j$, $x \in R^n$,

$f : \underbrace{R^n \times \cdots \times R^n}_{r \ times} \rightarrow R^n$ and $f(0, \cdots, 0) = 0$.

Definition 1: The origin $x_i = 0$, $i \in N$ of (65) is string stable, if given any $\epsilon > 0$, there exists a $\delta > 0$ such that $||x_i(0)||_\infty < \delta \Rightarrow sup_i ||x_i(\cdot)||_\infty < \epsilon$.

Definition 2: The origin of the interconnected system $x_i = 0$, $i \in N$ of (65) is asymptotically (exponentially) string stable if it is string stable and $x_i(t) \rightarrow 0$ asymptotically (exponentially) for all $i \in N$.

Theorem (Weak Coupling Theorem for String Stability)[12]: If the following conditions are satisfied:

- f is globally Lipschitz in its arguments, i.e.,

$$\begin{aligned} &|f(y_1, \cdots, y_r) - f(z_1, \cdots, z_r)| \\ &\leq l_1|y_1 - z_1| + \cdots + l_r|y_r - z_r|. \end{aligned} \tag{66}$$

- The origin of $\dot{x} = f(x, 0, \cdots, 0)$ is globally exponentially stable.

Then for sufficiently small l_i, $i = 2, \cdots, r$, the interconnected system is globally exponentially string stable.

The above theorem provides a sufficient condition for string stability of an interconnected system, and it shows that string stability can be achieved if the coupling between the system components is sufficiently weak.

For the steering control of the ith vehicle in autonomous vehicle following, the feedback signal is the vehicle's lateral distance from the preceding vehicle. Hence, by

neglecting the road curvature,

$$\dot{x_i} = Ax_i + B\delta_i \tag{67}$$

$$\delta_i = -Ky_{Li} \tag{68}$$

where K is the steering control gain. According to Eqn.(59),

$$\begin{aligned} \delta_i &= -K(y_{Vi} - y_{Ri-1}) \\ &= -K(C_2x_i - C_1x_{i-1}) \end{aligned} \tag{69}$$

Then,

$$\begin{aligned} \dot{x_i} &= Ax_i + B(-K(C_2x_i - C_1x_{i-1})) \\ &= (A - BKC_2)x_i + BKC_1x_{i-1} \\ &= g(x_i, x_{i-1}) \end{aligned} \tag{70}$$

It is clear from the above equations that the feedback control system of the ith vehicle is coupled with that of the $(i-1)$th vehicle, and hence the vehicle platoon forms an interconnected system. It can be shown that

$$\begin{aligned} &|g(y_1, y_2) - g(z_1, z_2)| \\ \leq &|A - BKC_2| \cdot |y_1 - z_1| + |BKC_1| \cdot |y_2 - z_2| \end{aligned} \tag{71}$$

The above expression shows that to make the coupling weak, the magnitude of the controller K has to be sufficiently small. Clearly, this is not a practical solution.

5.7 Inter-Vehicle Communication Based Approach

According to Eqn.(59), if the absolute position of the rear end of the $(i-1)$th vehicle y_{Ri-1} is known, the coupling between the ith and the $(i-1)$th vehicle vanishes. Measurements of y_{Ri-1} may become available to the $(i-1)$th vehicle, if the vehicle is equipped with appropriate sensors such as GPS, vision camera, or magnetometers. Then through inter-vehicle communication, measurements of a leading vehicle, e.g.the $(i-1)$th vehicle, are shared by all the following vehicles. The vehicle directly following the leading vehicle may compute

$$y_{Vi} \approx (y_{Li} - y_{Ri-1}) \tag{72}$$

Note that y_{V_i} is the lateral deviation, at a point with distance L ahead of vehicle CG, relative to the road centerline, and it does not depend on the preceding vehicle. Now the following vehicle may use y_{V_i} as the feedback signal to the control algorithm. Then, the tracking performance of the vehicle should not depend on that of the preceding vehicle.

Inter-vehicle communication between the vehicles was achieved through Utilicom radios. At constant time steps (every $20msec$), the lead vehicle sent its measurements of the rear magnetometers (under rear bumper) to the following vehicle. The lead vehicle was under automated steering control with the magnetometer measurements as the feedback signal, but the following vehicle used only LIDAR measurements and communicated information from the lead vehicle. The same H_∞ controller as described previously was used for the following vehicle. Again, due to technical difficulty, the leading vehicle only used the redesigned controller, which is in lead-lag form and generates a positive bias in tracking errors as shown in Figs.34 and 35, because synchronization was required in order to enable the communication process.

The experimental results of the autonomous vehicle following control with inter-vehicle communication are shown in Fig.38 and Fig.39. The results show that with inter-communication not only was the lateral deviation of the following vehicle significantly reduced, but also the bias disappeared. Note that the speed of the test vehicles was up to 25MPH, a little higher than that in the previous tests. The reason for performance improvement is that the control algorithm regulated the vehicle's absolute deviation, at the point L ahead of vehicle CG, from the road centerline, instead of the relative deviation from the lead vehicle. This was achieved by using inter-vehicle communication and combining LIDAR measurements with the communicated information.

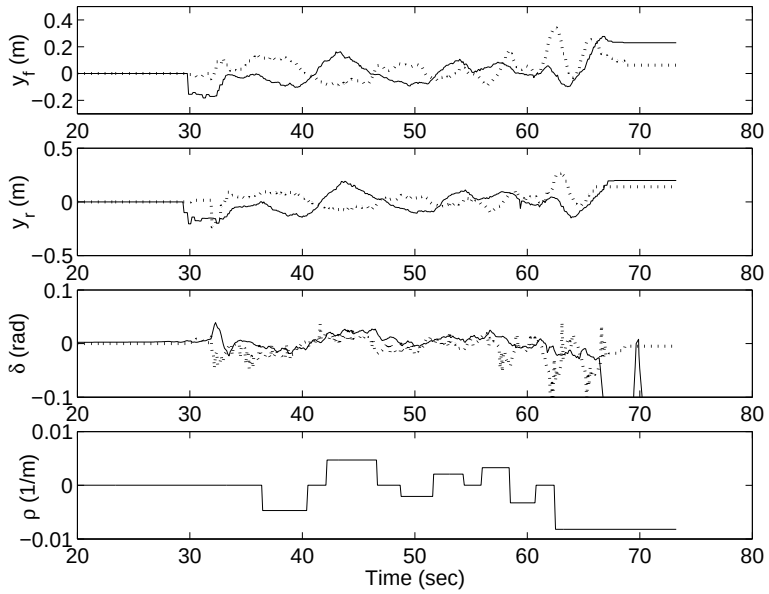

Figure 38: Experimental results for autonomous vehicle following with inter-vehicle communication: front, rear magnetometer outputs, steering angle, and road curvature. (solid: following vehicle; dashed: lead vehicle)

5.8 Simulation for a Vehicle Platoon

Simulations have been conducted to study the effects of inter-vehicle communication on vehicle performance and string stability for a larger vehicle platoon. Assuming that the 1st vehicle measures its absolute deviation y_{R1} and communicates it to the following vehicles, the second vehicle calculates y_{V2} by combining the communicated information with LIDAR measurements. However, since the second vehicle cannot measure y_{R2}, this algorithm stops and cannot be applied to the third vehicle. To solve the problem, a Kalman estimator is developed to estimate y_{R2} from y_{V2}. The problem is formulated for the ith vehicle as follows. For simplicity, the subscript i has been omitted.

$$\dot{x} = Ax + B\delta + Bw \tag{73}$$

$$y_V = C_2 x + v \tag{74}$$

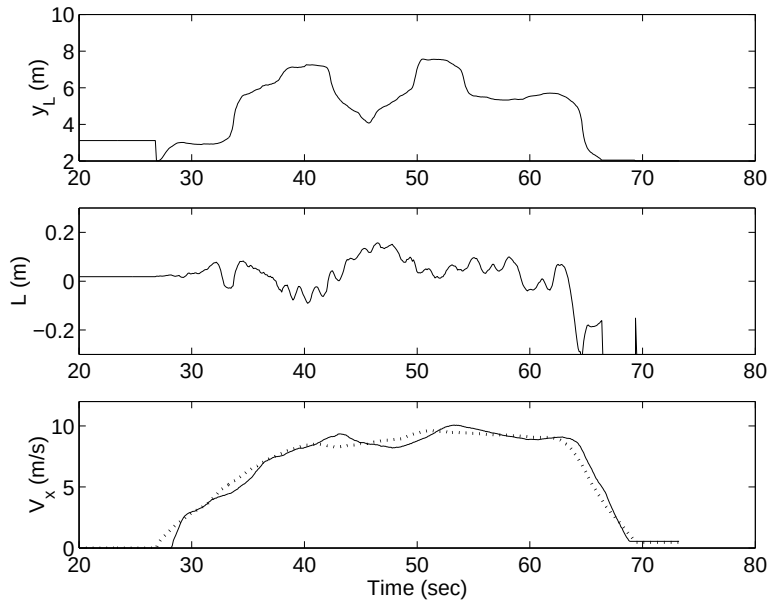

Figure 39: Experimental results for autonomous vehicle following with inter-vehicle communication: lateral, longitudinal distance between the two test vehicles measured by LIDAR, and vehicle speed (solid: following vehicle; dashed: lead vehicle)

where w is process noise, and v is measurement noise. The noise covariances are chosen as

$$E(ww') = 2.5e - 005; \tag{75}$$

$$E(vv') = 0.0004; \tag{76}$$

$$E(wv') = 0; \tag{77}$$

The estimator has input $[\delta; y_V]$, and it can compute the optimal estimate of the state variable $\hat{x}$. Clearly,

$$\hat{y_R} = C_1\hat{x} \tag{78}$$

Then the estimated $\hat{y_R}$ can be communicated to the following vehicles, and the previous algorithm continues in the upstream direction of the platoon. The soundness of estimating y_{R2} by using y_{V2} is validated using the measurements from the previous experiments, as shown in Fig.40. The figure shows that most of the time the estimation error is about 5 to $8cm$.

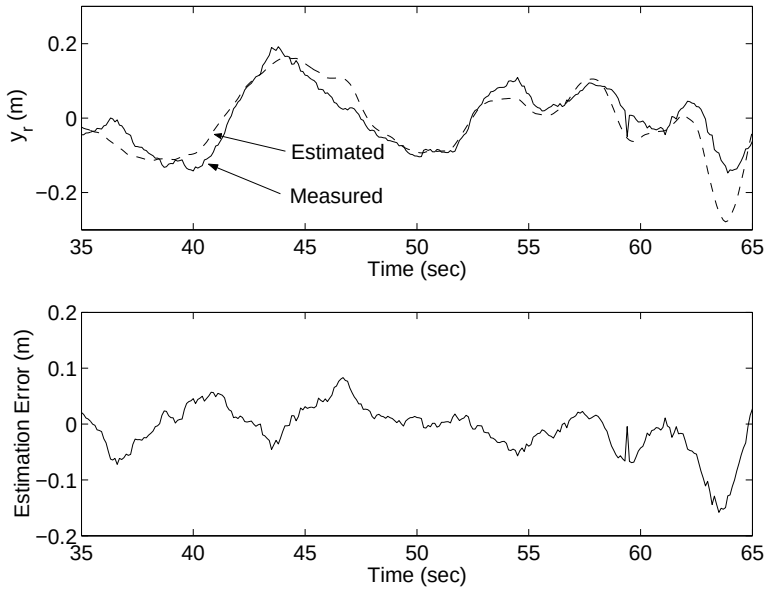

Figure 40: Estimation of y_R based on y_V and control input

The simulation used a platoon of four vehicles, under the same condition as described in Section 5.6. In the first simulation, it was assumed that y_R is perfectly estimated, and the simulation results are plotted in Fig.41 as lateral deviation at the vehicle CG vs. time. The results show that with inter-vehicle communication, the lateral errors of the all the following three vehicles are almost the same, and the errors no longer accumulate in the upstream direction of the platoon.

Since the above results may seem optimistic to some extent, simulations have been conducted again with the assumption that each estimator generates $10cm$ random error. The results are plotted in Fig.42. It can be seen that even with the random noise in the simulation the tracking errors of the following vehicle do not accumulate as much as in Fig.37. These results show that inter-vehicle communication is a practical way to solve the string stability problem in autonomous vehicle following.

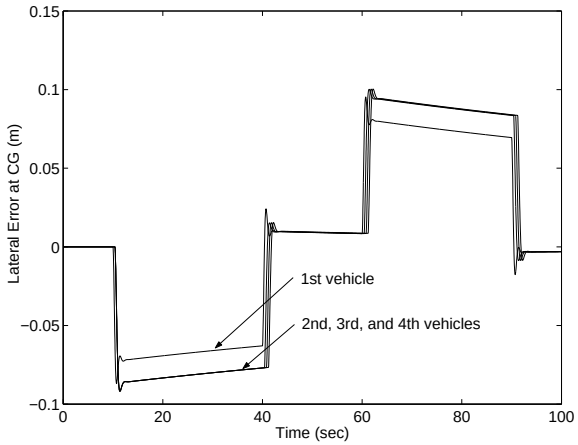

Figure 41: Simulation results for a platoon of four vehicles with perfect estimation

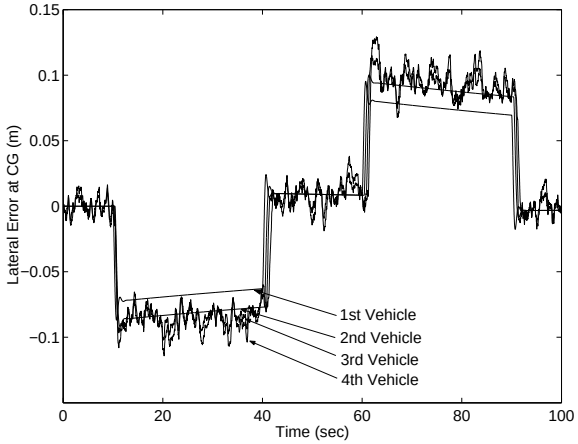

Figure 42: Simulation results for a platoon of four vehicles $10cm$ estimation error

5.9 Summary

This section presented a new scheme for autonomous vehicle following steering control of a passenger vehicle. Autonomous vehicle following allows a vehicle to automatically follow its preceding vehicle, based on real-time information of the relative distance between the two vehicles. In this work, the relative distance is measured by an on-board laser scanning radar sensor (LIDAR). Real-time testings were conducted on a test track which was equipped with a unique magnetic reference system. The error propagation problem in autonomous vehicle following was emphasized in this section, as it may eventually result in string instability of a vehicle platoon. This problem was demonstrated repeatedly through two real-time testing results and a simulation result of a platoon of four vehicles. The string stability problem was analyzed for autonomous following, and the inter-vehicle communication approach was suggested as a solution. The controller uses measurements from both LIDAR and the communicated lateral deviation of the leading vehicle. Experimental results were presented to show that inter-vehicle communication effectively reduced the vehicle tracking errors in autonomous following. Simulation results were also presented to confirm that inter-vehicle communication helps solve the string stability problem for a larger platoon of vehicles.

6 Integrated Steering Control

6.1 Introduction

In the previous section, it was shown that autonomous vehicle following may be used as an independent automatic steering control system. Hence it may work as a back-up system for road following control schemes during the total failure of magnetometers. Autonomous vehicle following may also become helpful to the road following schemes when the magnetometers partially fail. The current magnetometer-based vehicle con-

trol schemes rely on two sets of on-board magnetometers, mounted under the front and rear bumpers. Failure in either set of the magnetometers leads to degraded steering performance, sometimes even causing instability. As shown in previous research, front magnetometers are critical for vehicle lateral control. More precisely, if the front magnetometers fail, a right-half-plane zero appears on the pole-zero map of the input-output dynamics from the front wheel steering angle to the lateral error at the rear bumper, which may cause a substantial deterioration of the lane-keeping performance. However, the desired vehicle performance may be achieved by combining the rear magnetometers with the LIDAR sensor. Inclusion of the magnetometer measurements in vehicle following control may also reduce the dependence of the following vehicle on the lead vehicle. Under this integrated control scheme, the controlled plant, i.e. the vehicle, becomes a Single Input, Two Output (SITO) system: the front wheel steering angle is the input and the rear magnetometers and LIDAR define the two outputs. In the closed loop, disturbances associated with one system output may have strong effects on the other output. This may become a severe problem considering the strong disturbance associated with the LIDAR measurement, which is caused by the unknown dynamics of the leading vehicle. Freudenberg and Middleton[3] have proposed the concepts of "direction" and "alignment" in analyzing general SITO systems. This section will first analyze the interactions of the SITO systems, and then propose a controller design procedure to achieve minimum interactions as well as stability and optimal performance under failure of front magnetometers.

6.2 Problem Formulation and Control Objectives

When the front magnetometers fail, the back-up system may utilize the rear magnetometers and the LIDAR sensor. It should be noted that the measurements of the LIDAR sensor are relative to the coordinate system fixed to the lead vehicle, while those of the rear magnetometers are relative to the road reference coordinate system. For the road reference system, LIDAR measurements can be considered as

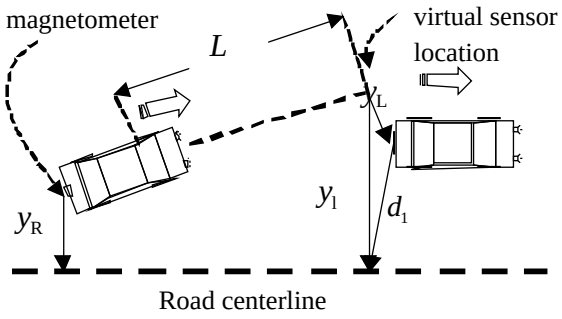

Figure 43: Geometry of sensor locations

the composition of two parts, i.e. the position of the following vehicle at the LIDAR measurement location and the position of the rear of the preceding vehicle. The latter part depends on the dynamics of the preceding vehicle. It is assumed in this section that there is no communication between the vehicles, and the dynamics of the preceding vehicle are considered as unknown disturbances. Hence, the system outputs can be written as $y = H\xi$, where

$$H = \begin{bmatrix} 1 & 0 & L & 0 \\ 1 & 0 & -h_2 & 0 \end{bmatrix}, \tag{79}$$

and y is the measured system output. The physical meanings of L and h_2 can be found in Table 1. The first system output in the above equations is the measurement from the LIDAR sensor and the second one is from the rear magnetometers. Figure 43 shows the geometry of the sensor locations and measurements. Note that the output equation assumes that the LIDAR output of the following vehicle is equivalent to the lateral error measured by a (virtual) sensor located at L $[m]$ ahead of the following vehicle's CG. Disturbance d_1 is introduced to absorb the discrepancy between this assumption and the actual situation. The dynamics of the preceding vehicle may affect d_1.

The control system is shown in Fig.44, where P is the Single Input, Two Output (SITO) plant, y_L is the output of the LIDAR sensor, d_1 is the disturbance as described above, and d_2 is the disturbance associated with the measurements from the rear set

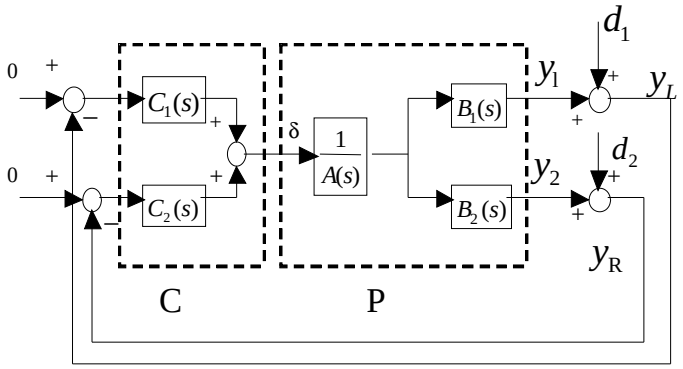

Figure 44: Control problem formulation

of magnetometers, y_R. As described in Section 6.1, vehicle lateral control performance with the feedback signal from the rear magnetometer measurements alone is limited because of an unstable zero of the vehicle dynamics from δ to y_R. The benefit of using the information from the LIDAR sensor is that the dynamics from δ to y_L do not involve any unstable zeros. In fact, the zero appears in the left-half side of the s-plane. However, the disadvantage of using the LIDAR sensor is that the disturbance, due to the unknown actual position and dynamics of the preceding vehicle, may affect the performance in terms of following the road centerline. Measurements from the rear magnetometers may be helpful in order to bring the vehicle back to the road centerline because they provide accurate measurements of the lateral deviation of the vehicle. The optimal way of combining these two sensor outputs can be achieved by careful controller design, based on the integrated closed loop system analysis. The control objective is to design a Two Input Single Output (TISO) controller such that no significant interactions occur in this closed loop control system within the system bandwidth, i.e., disturbances associated with one channel should have minimum effects on the other channel and vice versa. In particular, the effect of d_1 on the rear magnetometer loop should remain small. Moreover, the controller should internally stabilize the control system and achieve optimal closed loop system performance.

6.3 Properties of Single Input, Two Output Feedback Systems

In Fig.43, let

$$P(s) = \begin{bmatrix} p_1(s) \\ p_2(s) \end{bmatrix} = \begin{bmatrix} \frac{B_1(s)}{A(s)} \\ \frac{B_2 s}{A(s)} \end{bmatrix} \tag{80}$$

$$C(s) = \begin{bmatrix} c_1(s) & c_2(s) \end{bmatrix} \tag{81}$$

The output sensitivity function is

$$S_o(s) = \Big(\ I + P(s)C(s) \ \Big)^{-1} \tag{82}$$

Let

$$S_o(s) = \begin{bmatrix} S_{11} & S_{12} \\ S_{21} & S_{22} \end{bmatrix} \tag{83}$$

Then the system outputs are written as,

$$\begin{bmatrix} y_L(s) \\ y_R(s) \end{bmatrix} = S_o \begin{bmatrix} d_1(s) \\ d_2(s) \end{bmatrix} = \begin{bmatrix} S_{11}d_1 + S_{12}d_2 \\ S_{21}d_1 + S_{22}d_2 \end{bmatrix} \tag{84}$$

The above equation implies that d_1 affects y_R, and d_2 affects y_L, only through the off-diagonal terms of S_o. Therefore, it is important to minimize the magnitudes of these terms. In particular, S_{21} should remain small. The following theorem is summarized from the work done by Freudenberg and Middleton[3].

Theorem: For a fixed open loop gain $L = CP$, $max(|S_{21}|, |S_{12}|)$ is lower bounded, and the lower bound can be achieved iff

$$\frac{c_2(j\omega)}{c_1(j\omega)} = conj(\frac{p_2(j\omega)}{p_1(j\omega)}) \tag{85}$$

where $conj(x)$ represents the complex conjugate of x.

Proof: Let T_I be the complementary sensitivity function, i.e.

$$T_I = \frac{CP}{1 + CP} \tag{86}$$

Let

$$p_r = \frac{p_2}{p_1} \tag{87}$$

and

$$c_r = \frac{c_2}{c_1} \tag{88}$$

Then by applying the triangle inequality,

$$|S_{21}| \geq |T_I| \frac{|p_r|}{1 + |c_r p_r|} \tag{89}$$

and

$$|S_{12}| \geq |T_I| \frac{\frac{1}{|p_r|}}{1 + \frac{1}{|c_r p_r|}} \tag{90}$$

The equality holds if and only if $c_r p_r$ is real, i.e. $c_r = \alpha \bar{p}_r$, where α is a real number. It can be shown by comparing the two off-diagonal terms of S_o that $max(|S_{21}|, |S_{12}|)$ is lower bounded by $|T_I| \frac{|p_r|}{1+|p_r|^2}$, and the lower bound can be achieved if and only if α=1. End of proof.

More properties about SITO systems can be found in Freudenberg and Middleton[3], where the "alignment angle" is defined as

$$\phi(j\omega) = arccos(\frac{|C(j\omega)P(j\omega)|}{||C(j\omega)||.||P(j\omega)||}) \tag{91}$$

assuming that $P(j\omega) \neq 0$ and $C(j\omega) \neq 0$. The extent to which the two system outputs interact with each other can be quantified by using the alignment angle. It can be shown that $\phi(j\omega) = 0$ if and only if $\frac{c_2(j\omega)}{c_1(j\omega)} = conj(\frac{p_2(j\omega)}{p_1(j\omega)})$. Therefore, the lower bound as described in the above theorem is achieved if and only if the alignment angle is 0.

6.4 Proposed Controller Design Procedure

Based on the theorem described in the previous section, the proposed controller design procedure is as follows.

1. Determine a stable transfer function $W(s)$ which is the best approximation of $conj(\frac{p_1(j\omega)}{p_2(j\omega)})$, and define $c_1(s) = W(s)c_2(s)$. This will guarantee that the

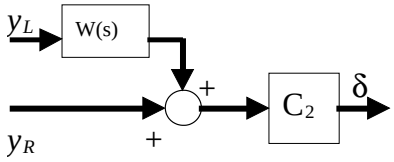

Figure 45: Formulation of controller

interactions between the system outputs as described in the previous section can be minimized.

2. Write $c_1(s)$ in terms of $c_2(s)$, absorb $W(s)$ into the plant, and convert the problem into a typical design problem for a SISO plant searching for c_2.

3. Choose suitable weighting functions, and apply conventional design techniques to find c_2, which minimizes the effects of the system disturbances on the regulated signals, such as lateral deviation and control input.

4. After c_2 is found, the controller C is formulated as shown in Fig.45.

Utilizing the parameter values in Table 1, $p_1(s)$ and $p_2(s)$ become

$$p_1(s) = \frac{536s^2 + 30720s + 18199}{s^4 + 75s^3 + 1135s^2} \tag{92}$$

$$p_2(s) = \frac{-41s^2 - 2454s + 18199}{s^4 + 75s^3 + 1135s^2} \tag{93}$$

The frequency responses of $p_1(s)$ and $p_2(s)$ are shown in Fig.46 and Fig.47. The weighting function is chosen to be

$$W(s) = \frac{-41s^2 - 2454s + 18199}{536s^2 + 30720s + 18199} \tag{94}$$

which implies that $conj(\frac{p_2(j\omega)}{p_1(j\omega)})$ is approximated by $\frac{p_2(j\omega)}{p_1(j\omega)}$. This approximation is valid at low frequencies as shown in Fig.48. The controller c_2 in step 3 has been designed

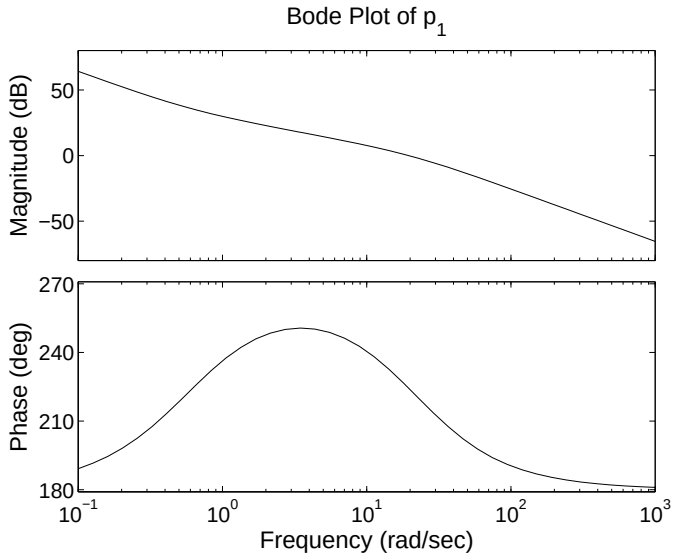

Figure 46: Bode plot of $p_1(s)$

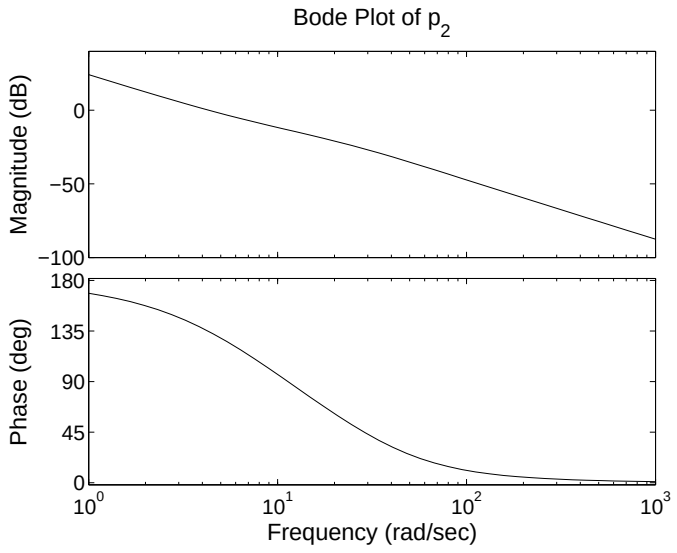

Figure 47: Bode plot of $p_2(s)$

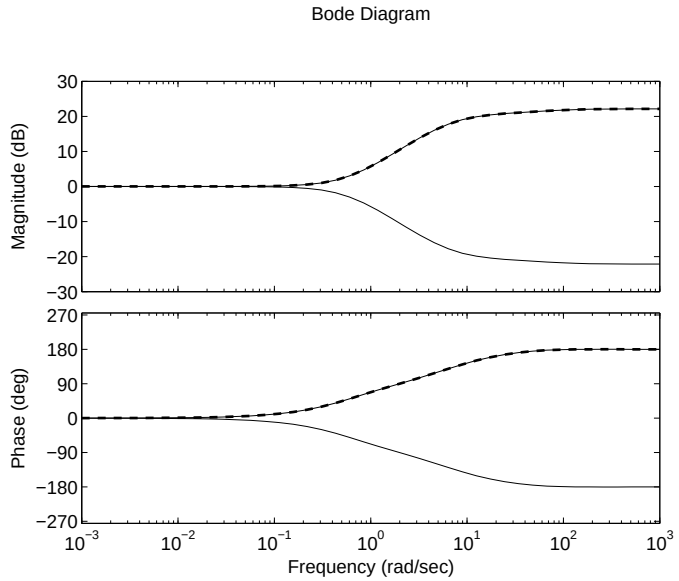

Figure 48: Frequency response of $W(j\omega)$ (solid) and $conj\{\frac{p_2(j\omega)}{p_1(j\omega)}\}$ (dashed)

by using H_∞ techniques and is shown as follows.

$$c_2(s) = \frac{\begin{array}{l} 0.09115s^8 + 23.03s^7 + 1953s^6 + 66476s^5 + 756354s^4 \\ +574700s^3 + 101610s^2 + 8802s + 25 \end{array}}{\begin{array}{l} s^9 + 152s^8 + 8298s^7 + 197922s^6 + 2242627s^5 + 12591485s^4 \\ +35914851s^3 + 17328941s^2 + 52962s + 3.897 \end{array}} \quad (95)$$

The TISO controller can be constructed using c_2 and $W(s)$ as shown in step 4. The frequency responses of c_2 and c_1 are shown in Fig.49 and 50 respectively. The alignment angle shown in Fig.51 is kept small at low frequencies.

6.5 Simulation Results

Simulations have been conducted on a platoon of four vehicles. The lead vehicle was under normal magnetometer-based control with two sets of magnetometers, and the three following vehicles were under the control algorithm described in the previous section, i.e., each of them utilized measurements from the LIDAR sensor and rear

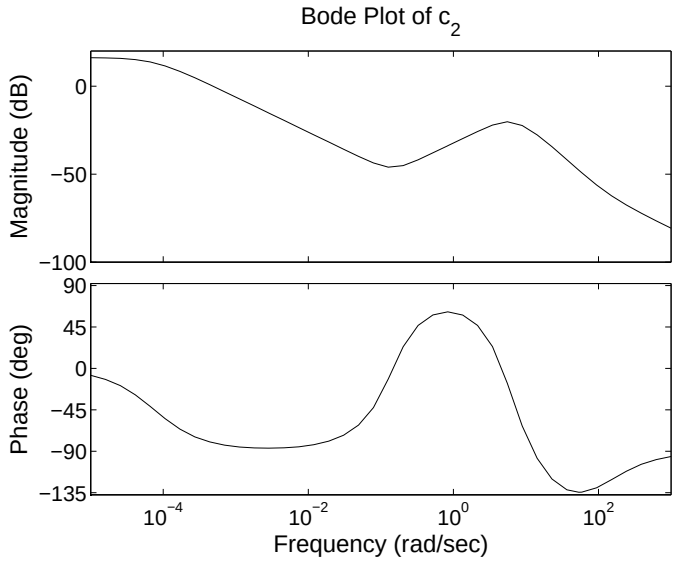

Figure 49: Frequency response of $c_2(s)$

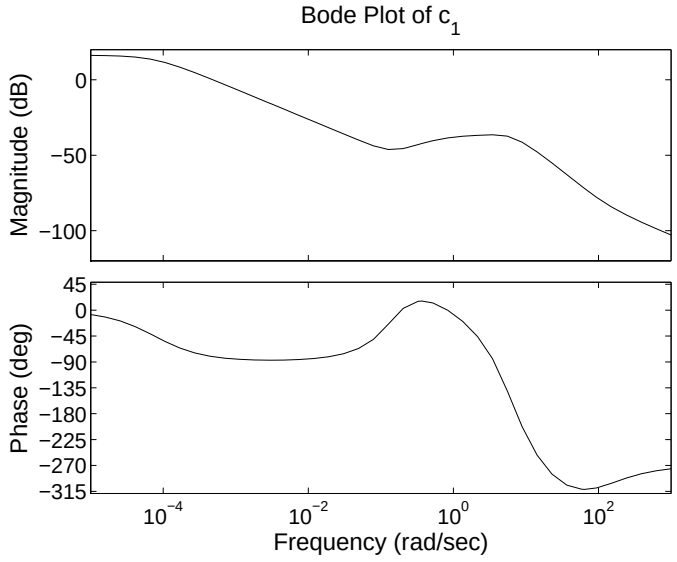

Figure 50: Frequency response of $c_1(s)$

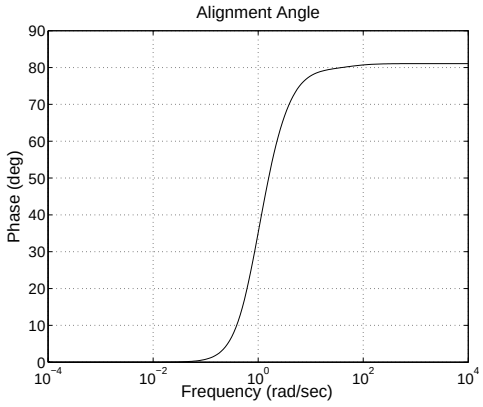

Figure 51: Alignment angle

magnetometers, pretending that the front magnetometers had failed. The longitudinal velocity used in the simulation increased from 20 m/s to 40 m/s and remained constant thereafter, as shown in Fig.52. Figure 53 shows the road curvature profile in the simulations. The simulated road consists of two curved sections, each having a constant road curvature of $\pm 1/800$ [1/m]. Figure 54 shows the simulation results. It is evident in the figure that the lateral deviation of each following vehicle is less than that of its preceding vehicle, although the three following vehicles were using exactly the same controller. It should be noted that the tracking performance would have been severely impaired if the feedback system had been obtained solely from the rear magnetometers.

6.6 Experimental Results

The weighting function and the 9th-order controller have been implemented and successfully tested on the same platoon of the two Buick vehicles on the same test track as in the previous testing in Section 5. The front vehicle was under automatic lateral control based on both the front and rear sets of magnetometers. In order to study the effects of different biases in the tracking error of the leading vehicle on that of the following vehicle, two different experiments were conducted, in which the leading

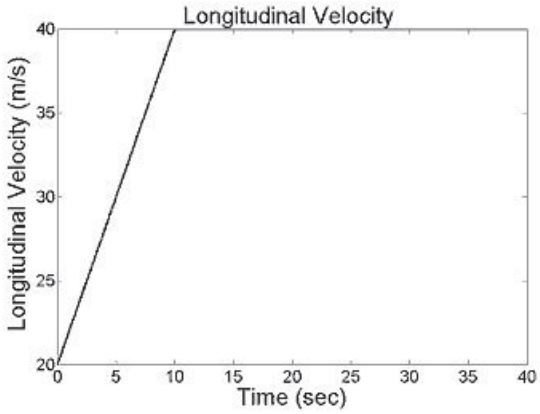

Figure 52: Longitudinal velocity profile

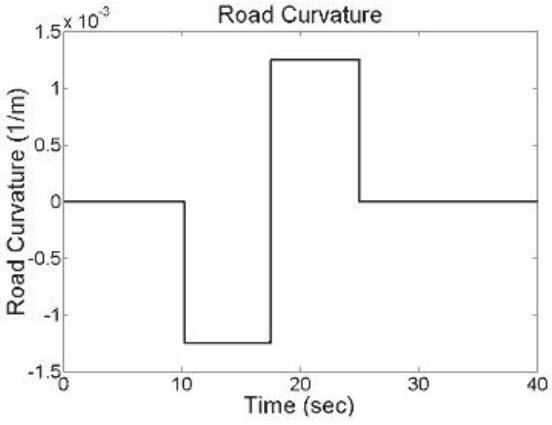

Figure 53: Road curvature profile

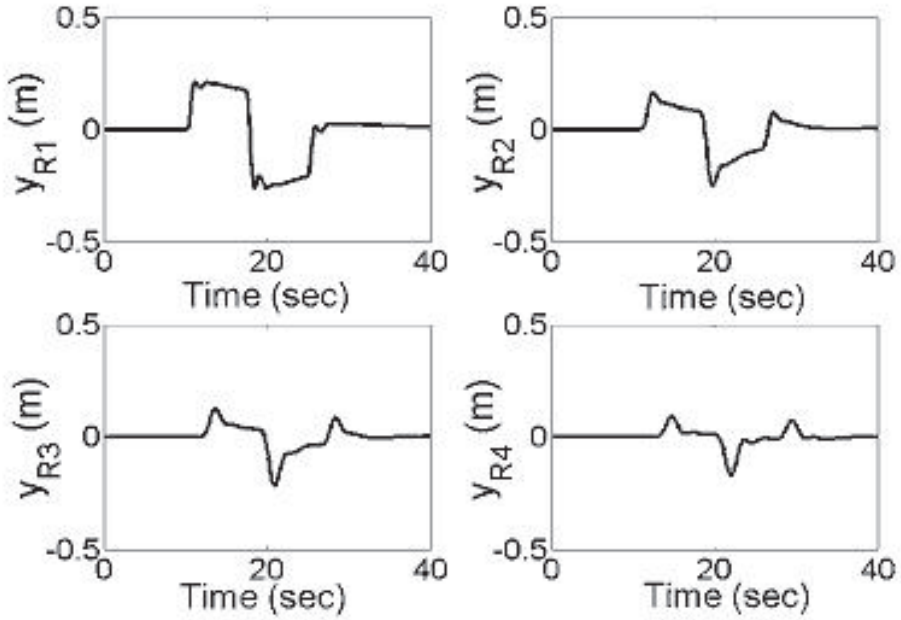

Figure 54: Lateral deviation of 4 vehicles in a platoon (y_{Ri} denotes the lateral deviation of the i th vehicle in the platoon measured by the rear magnetometers)

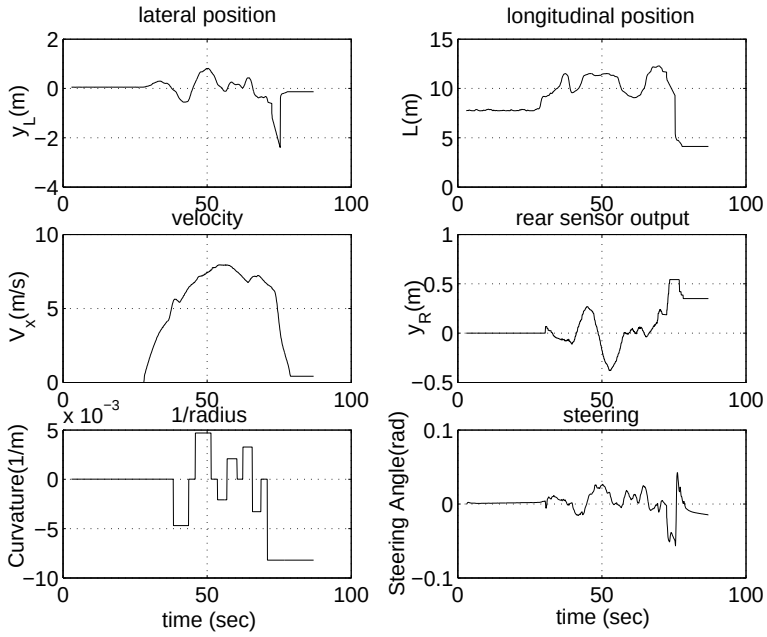

Figure 55: Experimental results of following vehicle with combined use of LIDAR and rear magnetometers when the tracking error of the leading vehicle has a negative bias: lateral and longitudinal distance measured by LIDAR sensor, vehicle velocity, rear magnetometer measurements, road curvature, and steering command

vehicle used the same two controllers as described in Section 5 respectively (the two magnetometer-based controllers which generated biases in opposite signs when string stability being studied in experiments). The following vehicle was controlled by the proposed 9th-order controller with combined use of LIDAR and rear magnetometer measurements in both experiments. The testing speed was up to 20MPH, and the distance between the two cars was manually maintained at about $10m$. The experimental results when the tracking error of the leading vehicle has a negative bias are shown in Fig.55. The experimental results of the lead vehicle are similar to Fig.32 since the lead vehicle was under the same controller as in the previous test, and hence are not shown here. The relative lateral and longitudinal position of the controlled vehicle with respect to the lead vehicle were measured by the LIDAR sensor, and the position of the controlled vehicle with respect to the road centerline was measured

by the rear magnetometer. The results show that by following both the lead vehicle and road centerline (with combined use of LIDAR and rear magnetometers), the controlled vehicle followed the road centerline with the maximum lateral error of about 35cm. The controller did not work well at the end of the test track, when the road curvature became over 0.008 $[1/m]$, which was not realistic for normal highways. The tracking error of this controller is less than that of the controller using just LIDAR in Section 5, since now the vehicle can "see" its deviation from the road centerline through the magnetometers, although they are mounted at the rear end.

The experimental results when the tracking error of the leading vehicle has a positive bias are shown in Figs.56 and 57. The tracking error of the leading vehicle was smaller than that in the previous testing, and this also resulted in smaller tracking error of the following vehicle. Recall that the two control laws of the leading vehicle generate opposite biases in the tracking error, the results show that the integrated control scheme has effectively reduced the magnification effects of the bias on the following vehicle.

It should be noted that the tracking performance would have been severely impaired if the feedback system had been obtained solely from the rear magnetometers as shown in Fig.58. In this case, the controller calculates the required steering angle at the front tires by using only the measurements of the tracking error at the rear end of the car. This makes the rear-magnetometer-based steering control more challenging, especially when the vehicle runs on a curved track. Adjustment of the steering angle can be made only after the vehicle enters or even after it passes the curve. This is the main reason for the oscillations shown in Fig.58. However, the oscillations disappear in Fig.55, when the controller combines the use of the rear magnetometers with LIDAR, which provides necessary look-ahead information.

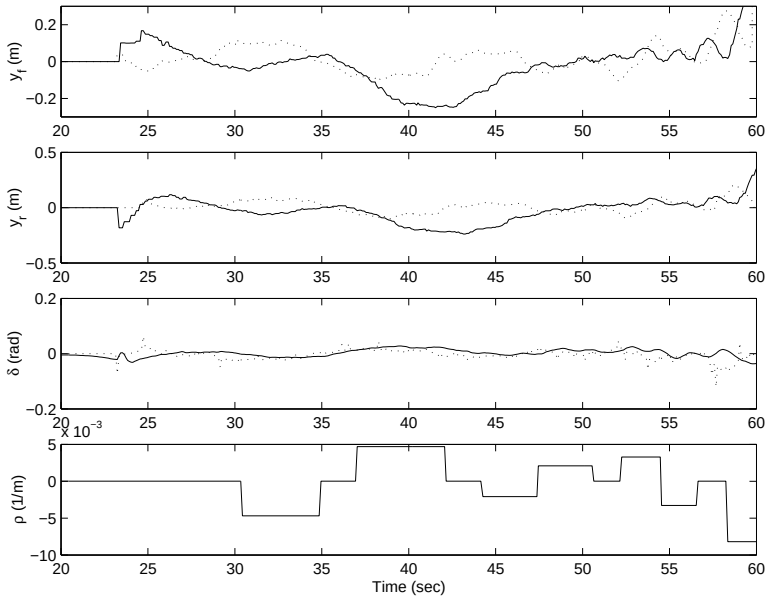

Figure 56: Experimental results of following vehicle with combined use of LIDAR and rear magnetometers when the tracking error of the leading vehicle has a positive bias: front, rear magnetometer outputs, steering angle, and road curvature. (solid: following vehicle; dashed: lead vehicle)

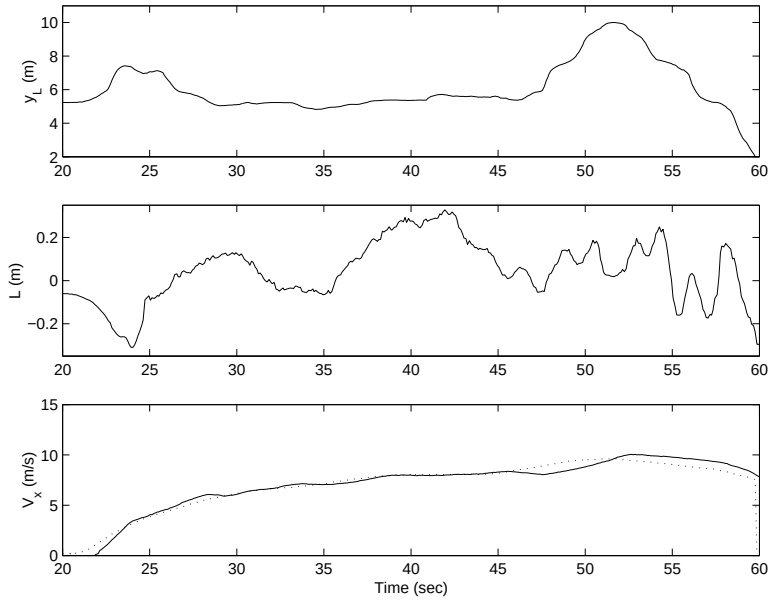

Figure 57: Experimental results of following vehicle with combined use of LIDAR and rear magnetometers when the tracking error of the leading vehicle has a positive bias: lateral, longitudinal distance between the two test vehicles measured by LIDAR, and vehicle speed (solid: following vehicle; dashed: lead vehicle)

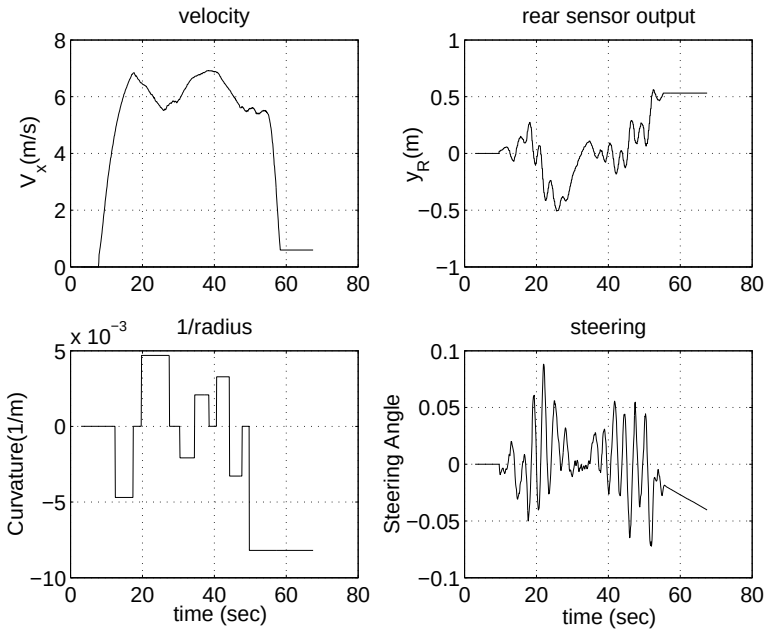

Figure 58: Experimental results of vehicle control using just rear magnetometers: vehicle velocity, rear magnetometer measurements, road curvature, and steering command

6.7 Summary

This section described the integrated steering control system that combined the LIDAR sensor and magnetometers. This is a mixture of autonomous vehicle following and the magnetometer-based road following approaches. The system may work as a backup system that deals with the partial failure of the on-board magnetometers. Especially this section considered the case of front magnetometers failure. The case of rear magnetometer failure is relatively easy to handle since the vehicle lateral dynamics define a minimum-phase system, and has not been discussed in this section. The controller design procedure is based on the minimization of the interactions of a single input, two output dynamic system for vehicle lateral control with combined use of the LIDAR sensor and the rear magnetometers. The design procedure guarantees good alignment of the plant and the controller within the closed loop bandwidth, ensuring no strong interactions in the closed loop system, i.e. the unknown actual position and dynamics of the preceding vehicle have little effects on the vehicle lane keeping performance. Two real-time testings have been conducted, in which the leading vehicle was controlled by the two different control algorithms respectively as used in the previous section. The two control laws generated small bias in the tracking error of the leading vehicle with opposite signs, but the results show that the integrated control system effectively reduced the bias in the tracking errors of the following vehicle.

7 Conclusions

This report focuses on the design of the vehicle lateral control systems under fault in front or/and rear magnetometers. Control algorithms have been developed for different magnetometer failure scenarios. The main results in the report are summarized as follows.

- Degraded mode controller design based on H_∞ optimal control techniques with gain scheduling

The analysis on the vehicle lateral dynamics with front or rear magnetometer measurements as the only output indicated that the main challenge in the control system design lies in the time varying property and the lack of phase due to magnetometer failures. H_∞ optimal control techniques were employed to achieve robustness to the variation of the vehicle lateral dynamics due to the change of the longitudinal velocity. However, a single H_∞ controller could not achieve robust performance in the whole operating range ($0 < v < 40m/s$), therefore, gain scheduling technique was introduced to extend the robust region. Both front-magnetometer-based (FMB) and rear-magnetometer-based (RMB) controllers were designed and simulation results showed the effectiveness of the controller design. However, the resulting control system involves switching among several H_∞ controllers and may not be optimal in terms of stability analysis and implementation simplicity.

- Degraded mode controller design based on feedback linearization and mismatched observer

  Feedback linearization with mismatched observer was proposed to address both the LTV property and the weakly damped zeros or the RHP zero in the FMB/RMB vehicle lateral dynamics. Feedback linearization provides a simple and effecive way of gain scheduling and the mismatch observer prevents the weakly damped zeros or the RHP zero of the vehicle lateral dynamics from being contained in the internal dynamics. Both FMB and RMB controllers were designed and the stability of the overall closed-loop system was examined using the concept of Quadratic Stability. For the designed linear time varying FMB controller, Quadratic Stability was achieved; however, for the RMB control, Quadratic Stability was achieved with several mismatched observers, i.e., gain scheduling was still involved. (It is not necessarily true that feedback linearization with mismatched observer is not suitable for any LTV system with RHP zeros.) Experiments were conducted at Richmond Field Station, and the results

demonstrated the effectiveness of the controller design.

- Transition behavior between non-faulty and faulty conditions
  Smooth transition behavior, along with a reliable FDI module and robust normal mode control and degraded mode control, is crucial for a successful fault tolerant control system. The transition behavior is affected by the delay in the FDI module and the robostness of the controllers before and after the transition. Switching mechanisms such as linear interpolation and Initial Value Compensation (IVC) were reviewed and the actual transition behavior between the normal mode controller and the degraded model controller was investigated. Both simulation and experiments showed that the transition behavior was quite smooth even with a direct switch in the control force; hence more complicate switching mechanisms are practically unnecessary. The benigh transition behavior is due to the robustness of both the normal mode controller and the degraded mode controller. The effects of delay was also investigated in experiments and the transition behavior is very smooth for up to at least 10 markers detection delay.

- Autonomous Vehicle following
  A new approach for vehicle steering control, i.e. autonomous vehicle following, has been studied. In this approach, a vehicle is automatically steered to follow its preceding vehicle. If the leading vehicle is running on the desired track, with small tracking errors, then the following vehicle may also achieve the lane-keeping control goal. This is an indirect lane-keeping control scheme, in the sense that the feedback signals of the closed-loop control system are not relative to the road centerline, but relative to another vehicle. The main benefit of this approach is that it does not rely on any road infrastructure, e.g. lane markers or magnetic markers, hence the system is easy to implement. It may work as an independent driver assistant system, or be combined with a cruise control system to achieve full automated control of a vehicle.

The most significant challenge in developing autonomous vehicle following controllers is the inter-connected feature built in this scheme. The existence of a leading vehicle is required, and the following vehicle can only follow the trajectory of the leading vehicle. This constraint may not be a problem for vehicles which run in platoons, e.g. groups of commercial heavy trucks having the same destination or passenger cars who are willing to run in groups. However, the tracking performance of the following vehicles largely depends on that of the leading vehicle because of the inter-connected feature. The tracking error of the leading vehicle is always transmitted to the following vehicles, and in general the tracking performance of the following vehicles becomes even worse. As the number of vehicles in the platoon increases, the tracking error of the very last vehicle may be unacceptably large. Because all vehicles are inter-connected, the stability of a single vehicle cannot guarantee the stability of the whole platoon. Hence analysis of the string stability problem becomes inevitable. The string stability problem may be solved in two ways. First, if the leading vehicle is equipped with some road following sensors, e.g. vision sensors, magnetometers, or GPS, communication of the measurements of these sensors to the following vehicles may help reduce the tracking errors of the following vehicles. Second, if all vehicles in the platoon has some kind of road following sensors, even if their measurements are not good enough to enable an effective road following system, the string stability problem may still be solved by incorporating these sensor outputs into the autonomous vehicle following system. Essentially, both methods weaken the coupling between every two adjacent vehicles so that the inter-connected feature in autonomous vehicle following can be removed.

- Integrated Vehicle Control with Combined Use of LIDAR and Magnetometers
  Autonomous vehicle following may become helpful to the magnetometer-based road following systems in the case when one set of the magnetometers have failed. Especially, the more challenging case of front magnetometer failure was

considered. Steering control with only the rear magnetometers is hard to realize because the input-output dynamics define a non-minimum phase plant. A back-up control system has been developed to combine the use of LIDAR with rear magnetometers to deal with the case of front magnetometer failure. The controller design principle was based on the minimization of the interactions of a single input, two output dynamic system for closed-loop vehicle lateral control with combined use of the LIDAR sensor and the rear magnetometers. The design procedure guaranteed good alignment of the plant and the controller within the closed loop bandwidth, ensuring no strong interactions in the closed loop system, i.e. the unknown actual position and dynamics of the preceding vehicle have little effects on the vehicle lane keeping performance. In general, such a solution may also become useful in dealing with other control problems, where two independent sensors are used, but interaction in the closed loop is of major concern.

Acknowledgement

This project is sponsored by California PATH (Partners of Advanced Transit and Highways) program. The contents of this report reflect the views of the authors who are responsible for the facts and the accuracy of the data presented herein. The contents do not necessarily reflect the official views or policies of the state of California. This report does not constitute a standard, specification, or regulation. We also acknowledge the technical contributions of Dr. H-S. Tan, D. Nelson, and other researchers at Richmond Field Station.

References

[1] B.R. Barmish, "Necessary and Sufficient Conditions for Quadratic Stabilizability of an Uncertain System", *Journal of Optimization Theory and Applications*, 1985, Vol. 46, 399-408

[2] Y. Bar-Shalom and T. E. Fortmann, "Tracking and Data Association", Academic Press, Inc., New York, NY, 1988

[3] J. Freudenberg and R. Middleton, "Properties of single input, two output feedback systems", *International Journal of Control*, 1999, Vol. 72, No. 16, 1446-1465

[4] T. Fujioka and M. Omae, "Vehicle following control in lateral direction for platooning", *Vehicle System Dynamics Supplement 28* (1998), pp. 422-437

[5] S. Gehrig and F. Stein, "A Trajectory-Based Approach for the Lateral Control of Car Following Systems", *Proceedings of the Intelligent Vehicles Symposium '98*, pp. 3596-3601, 1998.

[6] J. Guldner, H-S Tan. and S. Patwardhan. (1997). "Study of Design Directions for Lateral Vehicle Control", *Proceedings of the 36th Conference on Decision and Control*, San Diego, California USA, December 1997.

[7] P. Hingwe, and M. Tomizuka, "Robust and gain scheduled H_∞ controllers for lateral guidance of passenger vehicles in AHS", *Proceedings of the ASME Dynamic Systems and Control Division*, DSC-Vol. 61, November 1997, pp. 707-713

[8] P. Hingwe, A. Packard, and M. Tomizuka, "Linear Parameter Varying Controller for Automated Lane Guidance-Experimental Study on Tractor Semi-Trailers", *Proceedings of the American Control Conference*, Chicago, Illinois, 2000, pp. 2038-2042

[9] S. Ibaraki and M. Tomizuka, "H-infinity Optimization of Fixed Structure Controllers", *Proceedings of the International Mechanical Engineering Congress and Exposition*, Orlando, FL, 2000.

[10] V.K.Narendran and J.K.Hedrick, "Autonomous Lateral Control of Vehicles in an Automated Highway System", *Vehicle System Dynamics Supplement 23* (1994), pp. 307-324

[11] S. Patwardhan, H-S Tan. and J. Guldner. (1997). "A general Framework for Automatic Steering Control: System Analysis", *Proceedings of the American Control Conference*, Albuquerque, New Mexico, June 1997.

[12] D. Swaroop and J. K. Hedrick, "String Stability of Interconnected Systems", *IEEE Transaction on Automatic Control*, Vol. 41, No. 3, March 1996

[13] M. Vidyasagar, *Nonlinear System Analysis* (1978), Prentice-Hall.

[14] F. Wu, 1995, "Control of Linear Parameter Varying Systems", *PH. D. Dissertation*, Department of Mechanical Engineering, University of California, Berkeley.

[15] T. Yamaguchi, K. Shishida, H. Hirai, K. Tsuneta, and M. Sato, "Improvement of servo robustness for digital sector servo systemM", *IEEE Transaction on Magnetics*, Vol. 28, pp.2910-2912, 1992

[16] T. Yamaguchi, K. Shishida, S. Tohyama, and H. Hirai, "Mode switching control design with initial value compensation and its application to head positioning control on magnetic disk drives", *IEEE Transaction on Industrial Electronics*, Vol. 43, pp.65-73, 1996

[17] T. Yamaguchi, Y. Soyama, H. Hosokawa, K. Tsuneta, and H. Hirai, "Improvement of settling response of disk drive head positioning servo using mode switching control with initial value compensation", *IEEE Transaction on Magnetics*, Vol. 43, pp.1767-1772, 1996